Inertial thin film flow on planar surfaces featuring topography

S Veremieiev, H M Thompson, Y C Lee, P H Gaskell
School of Mechanical Engineering
University of Leeds
Leeds, LS2 9JT, UK

August 18, 2015

Abstract

A range of problems is investigated, involving the gravity-driven inertial flow of a thin viscous liquid film over an inclined planar surface containing topographical features, modelled via a depth-averaged form of the governing unsteady Navier-Stokes equations. The discrete analogue of the resulting coupled equation set, employing a staggered mesh arrangement for the dependent variables, is solved accurately using an efficient full approximation storage (FAS) algorithm and a full multigrid (FMG) technique; together with error-controlled automatic adaptive time-stepping and proper treatment of the associated nonlinear convective terms. An extensive set of results is presented for flow over both one- and two-dimensional topographical features, and errors quantified via detailed comparisons drawn with complementary experimental data and predictions from finite element analyses where they exist. In the case of onedimensional (spanwise) topography, moderate Reynolds numbers and shallow/short topographical features, the results obtained are in close agreement with corresponding finite element solutions of the full free-surface problem. For the case of flow over two-dimensional (localised) topography, it is shown that the free-surface disturbance is influenced significantly by the presence of inertia leading, as in the case of spanwise topography, to an increase in the magnitude and severity of the resulting capillary ridge and trough formations: the effect of inclination angle and topography aspect ratio are similarly explored.

1 Introduction

Numerous manufacturing processes require the deposition of thin liquid films, involving a balance between viscous and surface tension forces, on a variety of surfaces. In the coating industries for example, several devices exist which have been optimised specifically for the continuous production and fast throughput of uniform, defect free, films on flat homogeneous substrates, made from plastic, metal, paper, etc. These encompass a wide range of applications and about which much of the underpinning basic science is now reasonably well documented [1].

In contrast, the problem of thin film flow on surfaces containing man-made, micro-scale topographical features, with a pre-determined functionality, such as displays, printed circuits and sensors, is less well understood. Indeed, the areas in which such flow is encountered are endless, encompassing latterly the rapidly evolving area of microfluidics, see for example [2], and the need to manipulate flow on an ever decreasing scale in the context of lab-on-chip

devices. In addition, one should not forget the consequence(s) associated with the presence of unwanted surface topography, contaminates such as dust specks or irregularities resulting from a particular stage in a manufacturing process.

From a traditional standpoint the overall goal might arguably be one of identifying the parameters that influence the planarity of such films and thus guide its effective control, which represents a considerable challenge in itself given the diversity and nature of the surface topography encountered in practice. On the other hand, the realisation that naturally occurring surface patterns, regular and randomly distributed, are a key feature of numerous biological systems provides a different impetus; thin liquid films being important in areas as diverse as the redistribution of liquid lining the lung [3], plant disease control [4], biofilms [5] and water snail locomotion [6]. Plus the strong driver towards ultimately mimicking the behaviour of nature's surfaces [7], has brought the subject of film flow over topography into even sharper focus.

Accurate prediction of the associated three-dimensional freesurface flow by solving the governing unsteady Navier-Stokes (N-S) equations remains elusive; not from the standpoint of being unable to develop suitable discrete analogues, simply that the computational resource required to solve them is currently prohibitive. Accordingly, the bulk of the theoretical work that has appeared to date has relied on the assumption that creeping flow conditions prevail allied to the fact that for many thin film flows the ratio of the undisturbed asymptotic film thickness to that of the characteristic in-plane length-scale of the flow is small. Accordingly, if the velocity and pressure fields are expanded in terms of this small parameter and substituted into the N-S equations [8] then, retaining leading order terms, a fourth-order nonlinear degenerate partial differential equation for the film thickness, referred to as the lubrication approximation, results.

It is no surprise that the above long-wave approximation has proved popular, and the equations involved solved using a variety of numerical methods, with semi-implicit, alternating direction, time-splitting schemes [9, 10] enjoying wide usage. The argument used for employing such schemes is that they combine some of the stability properties of implicit schemes with the cost efficiency of explicit ones. However, when fine meshes are required to ensure mesh independent solutions the choice of time-step is severely restricted. With this in mind an investigation concerning droplet motion underpinned by lubrication theory [11] showed that the alternative approach of adopting a fully implicit multigrid formulation to: (i) be more robust; (ii) return an order of magnitude improvement in the rate of convergence for the levels of grid refinement required for accuracy; and (iii) utilise far less memory. The point was reinforced by Gaskell et al. [12] who combined the same multigrid approach with error-controlled adaptive timestepping. This same solution strategy was used in a detailed study of the flow of gravity-driven thin liquid films on non-porous substrates with topography, showing that the long-wave approximation leads to very good solutions, even in regions of parameter space where it is not strictly valid [13]. The methodology has subsequently been refined to embody error-controlled automatic mesh adaption [14, 15], leading to significant further improvement in solution times without loss of accuracy, and the inclusion of additional physics such as evaporation [16].

In addition and from the point of view of completeness it is important to mention that for Stokes flow the boundary element method has proven effective as a means of investigating threedimensional continuous thin film flow over a small particle adjacent to a flat surface [17, 18]. A Stokes flow perturbation analysis has also been used to study the particular case of gravity-driven flow over doubly-periodic surface corrugations, and extended to consider cases with finite Reynolds number [19, 20].

Unfortunately, few complementary experimental investigations involving thin film flow over discrete, steep topographical features have appeared in the literature affording direct comparison with theory, due to the formidable practical challenges involved. Early examples, featuring complementary long-wave analyses, include [21, 22, 23] and [24] who considered radial outflow

during spin coating and gravity-driven flow down an inclined plane, respectively. A key finding by both sets of authors was that lubrication theory proved surprisingly accurate for their modelling purposes; in addition [23] are credited as being the first to obtain a one-dimensional analytic expression for the standing capillary wave which forms at the leading edge of a trench topography and its associated downstream exponential decay. This problem was subsequently revisited by Fernandez-Parent et al. [25]; their Green's function formulation showed good agreement, with the second order term contained therein having the effect of locating the capillary ridge further upstream of the topography the deeper the trench. In a similar vein, Peurrung and Graves [26, 27] have reported both experimental and numerical results for spin coating that are in qualitative agreement. Considerable time then lapsed before a more useful batch of experimental data materialised [28, 29, 30]; culminating ultimately in the results presented by D*écré* and Baret [31] and which arguably currently form the experimental benchmark against which predictions may be compared.

As an alternative to employing lubrication theory, the influence of inertia for the particular case of gravity driven two-dimensional film flow over a plane containing steep spanwise topography only, has begun to be explored in terms of the so-called integral-boundary-layer approximation, a key feature of which is the assumption that the velocity profile across the film is parabolic. Its mathematical formulation, in which the resulting equations are expressed in terms of the film thickness and mean flow rate, can be traced back to Shkadov [32, 33] who used it to predict solitary waves in a thin viscous liquid layer on a uniform vertical surface. Recently, Saprykin et al. [34] extended the above idea to explore the influence of inertia and viscoelasticity on a thin film falling down such a surface and encountering a steep step-down topography. Of particular interest to them was examining the interaction between capillary ridges and excited non-equilibrium inertia/viscoelasticity-driven solitary pulses. Another approach worth mentioning is the depth averaged kinetic energy balance or energy integral method based on a velocity weighted average of the N-S equations was offered by Usha 2004 [39]. It is shown to be a reasonable alternative to a standard IBL avaraging of the N-S equations. Following a different path, Bontozoglou and Serifi [40] carried out a numerical investigation of the flow of a thin film down a plane containing steep step topography, once again in vertical alignment. They solved the steady-state form of the full N-S equations using a finite element method, showing that for large capillary numbers increasing inertia first amplifies and then diminishes the capillary features - an effect that would be difficult to capture with the integral-boundary-layer approach which is valid for small capillary numbers only.

Although not considered here, it is essential not to lose sight of the fact that inertial effects cause the free-surface flows of interest to become unstable when the Reynolds number exceeds a critical value; several analyses of the instability mechanism for the case of laminar flow down an inclined uniform surface have emerged, see for example [41, 42, 43], but very few have appeared that consider the influence of topography. Recent experiments have demonstrated, however, that there is a strong coupling between inertia and topography in gravity-driven flow over surfaces containing periodic rectangular corrugations [44] or wavy undulations [45]. The significant rise in critical Reynolds number that occurs due to the presence of surface topography, as observed experimentally, has also been predicted theoretically [46]. Recently, Trifonov [47] examined the stability of a viscous film flowing over a vertically aligned wavy surface, showing that there is a region of corrugation geometry (amplitude and period) where disturbances decay resulting in a stabilising effect, outside this region the flow is unstable. In addition, the reader is directed to the work of Khayat et al. [50] who provide a detailed account of the influence of inertia, topography and gravity on transient axisymmetric thin film flow, and to the recent investigations by Wierschem et al. [48] and Heining et al. [49] in connection with resonance effects in viscous films on inclined wavy planes.

The approach adopted in the present work involves the efficient solution of a depth-averaged form, akin to the integral-boundary-layer approximation, of the governing unsteady N-S equations: in particular, in the case of the three-dimensional flow associated with thin films encountering steep, localised topography. The mathematical formulation and solution strategy implemented to achieve accurate mesh-independent solutions of the reduced equation set are provided in Sections 2 and 3, respectively. A comprehensive set of results is presented in Section 4, including comparison of computed free-surface profiles with experimental data and corresponding finite element solutions of the full freesurface problem where they exist. Conclusions are drawn in Section 5.

2 Mathematical Formulation

Consider, as illustrated in Fig. 1, the case of time-dependent gravity-driven thin film flow down a planar surface containing a trench topography of depth S_0, length L_T and spanwise width W_T, that is inclined at an angle $\theta(\neq 0)$ to the horizontal. The liquid is assumed to be incompressible and to have constant density, ρ, viscosity, μ, and surface tension, σ. The chosen Cartesian streamwise, X, spanwise, Y, and normal, Z, coordinates are as indicated and the solution domain bounded from below by the planar surface, $Z = S(X, Y)$, from above at time T by the free-surface, $Z = F(X, Y, T)$, upstream and downstream by the inflow, $X = 0$, and outflow, $X = L_p$, planes, respectively, and to the left and right by the side planes at $Y = 0$ and $Y = W_p$. The film thickness, $H(X, Y, T)$, at any point in the (X, Y) plane at time T is given by $H = F - S$. The resulting laminar flow is described by the N-S and continuity equations, namely:

$$\rho\left(\frac{\partial \boldsymbol{U}}{\partial T} + \boldsymbol{U}\cdot\nabla\boldsymbol{U}\right) = -\nabla P + \nabla\cdot\boldsymbol{T} + \rho\boldsymbol{G}, \tag{1}$$

$$\nabla\cdot\boldsymbol{U} = 0, \tag{2}$$

where $\boldsymbol{U} = (U, V, W)$ and P are the fluid velocity and pressure, respectively; $\boldsymbol{T} = \mu\left(\nabla\boldsymbol{U} + (\nabla\boldsymbol{U})^T\right)$ is the viscous stress tensor, $\boldsymbol{G} = g_0(\sin\theta, 0, -\cos\theta)$ is the acceleration due to gravity where g_0 is the standard gravity constant.

Taking the reference length-scale in all directions to be the asymptotic, or fully developed, film thickness, H_0, and scaling the velocities by the free-surface (maximum) velocity, $U_0 = \rho g_0 H_0^2 \sin\theta/2\mu$ apropos the classic Nusselt solution [51], pressure (stress tensor) by $P_0 = \mu U_0/H_0$ and the time by $T_0 = H_0/U_0$, equations (1) and (2) can be rewritten in non-dimensional form as:

$$\mathrm{Re}\left(\frac{\partial \boldsymbol{u}}{\partial t} + \boldsymbol{u}\cdot\nabla\boldsymbol{u}\right) = -\nabla p + \nabla\cdot\boldsymbol{\tau} + \mathrm{St}\boldsymbol{g}, \tag{3}$$

$$\nabla\cdot\boldsymbol{u} = 0, \tag{4}$$

where $\boldsymbol{u} = (u, v, w)$, $\boldsymbol{\tau}$ and $\boldsymbol{g} = \boldsymbol{G}/g_0$ are the non-dimensional velocity, viscous stress tensor and gravity component, respectively; x, y, z, h, s, f, t, p together with s_0, l_t, w_t, l_p, w_p correspond to their dimensional counterparts. $\mathrm{Re} = \rho U_0 H_0/\mu$ is the Reynolds number and $\mathrm{SSt} = 2/\sin\theta$ the Stokes number; alternatively, the latter can be written as $St = Re/Fr^2$, where $Fr = U_0/\sqrt{H_0 g_0}$ is the Froude number.

The general problem definition is complete following the specification of appropriate no-slip, inflow, kinematic, free-surface normal and tangential stress boundary conditions [52]:

$$\boldsymbol{u}|_{z=s} = 0, \tag{5}$$

$$\boldsymbol{u}|_{x=0} = (z\,(2-z)\,,0,0)\,, \tag{6}$$

$$\frac{\partial f}{\partial t} + u|_{z=f}\frac{\partial f}{\partial x} + v|_{z=f}\frac{\partial f}{\partial y} - w|_{z=f} = 0, \tag{7}$$

$$-p|_{z=f} + (\boldsymbol{\tau}|_{z=f}\cdot\boldsymbol{n})\cdot\boldsymbol{n} = \frac{\kappa}{\mathrm{Ca}}, \tag{8}$$

$$(\boldsymbol{\tau}|_{z=f}\cdot\boldsymbol{n})\cdot\boldsymbol{t} = 0, \tag{9}$$

where $\mathrm{Ca} = \mu U_0/\sigma$ is the capillary number, $\boldsymbol{n} = \left(-\frac{\partial f}{\partial x}, -\frac{\partial f}{\partial y}, 1\right)\cdot\left[\left(\frac{\partial f}{\partial x}\right)^2 + \left(\frac{\partial f}{\partial y}\right)^2 + 1\right]^{-1/2}$ is the unit normal vector pointing outward from the free surface, $\boldsymbol{t} = \left(\alpha_t, \beta_t, \alpha_t\frac{\partial f}{\partial x} + \beta_t\frac{\partial f}{\partial y}\right)\cdot\left[\alpha_t^2 + \beta_t^2 + \left(\alpha_t\frac{\partial f}{\partial x} + \beta_t\frac{\partial f}{\partial y}\right)^2\right]^{-1/2}$ is the unit vector tangential to the free surface, α_t, β_t are variables that define the direction of the vector at any point in the tangent plane and $\kappa = -\nabla\cdot\boldsymbol{n}$ is the free-surface curvature.

2.1 Mathematical formulation

Although in principle the above system of equations and boundary conditions, (3)-(9), could be solved for the problem of interest using, for example, an appropriate finite element formulation, the memory and computational resources required to obtain the accuracy necessary to produce mesh independent solutions remains a formidable stumbling block. In addition, this constraint becomes further exacerbated, even in the Stokes flow limit, when one has to handle very small topographical features and/or when the same are sparsely distributed [14]. The task is simplified greatly by adopting a long-wave approximation [8], effectively reducing the dimensionality of the problem by one; the main assumption being that e $\varepsilon = H_0/L_0 \ll 1$, where L_0 is the characteristic in-plane length scale.

Formulating the governing equations (3) and (4) in terms of L_0 is equivalent to the following change of non-dimensional variables $(x, y, l_t, w_t, l_p, w_p, t, p) \rightarrow (x, y, l_t, w_t, l_p, w_p, t, p)/\varepsilon$, $w \rightarrow \varepsilon w$, leading to:

$$\varepsilon\mathrm{Re}\left(\frac{\partial u}{\partial t} + u\frac{\partial u}{\partial x} + v\frac{\partial u}{\partial y} + w\frac{\partial u}{\partial z}\right) = -\frac{\partial p}{\partial x} + \varepsilon^2\left(\frac{\partial^2 u}{\partial x^2} + \frac{\partial^2 u}{\partial y^2}\right) + \frac{\partial^2 u}{\partial z^2} + 2, \tag{10}$$

$$\varepsilon\mathrm{Re}\left(\frac{\partial v}{\partial t} + u\frac{\partial v}{\partial x} + v\frac{\partial v}{\partial y} + w\frac{\partial v}{\partial z}\right) = -\frac{\partial p}{\partial y} + \varepsilon^2\left(\frac{\partial^2 v}{\partial x^2} + \frac{\partial^2 v}{\partial y^2}\right) + \frac{\partial^2 v}{\partial z^2}, \tag{11}$$

$$\varepsilon^3\mathrm{Re}\left(\frac{\partial w}{\partial t} + u\frac{\partial w}{\partial x} + v\frac{\partial w}{\partial y} + w\frac{\partial w}{\partial z}\right) = -\frac{\partial p}{\partial z} + \varepsilon^4\left(\frac{\partial^2 w}{\partial x^2} + \frac{\partial^2 w}{\partial y^2}\right) + \varepsilon^2\frac{\partial^2 w}{\partial z^2} - 2\varepsilon\cot\theta, \tag{12}$$

$$\frac{\partial u}{\partial x} + \frac{\partial v}{\partial y} + \frac{\partial w}{\partial z} = 0, \tag{13}$$

while the boundary conditions (8) and (9) become:

$$-p|_{z=f} + \left\{\frac{2\varepsilon^2\left(-\frac{\partial u}{\partial z}\frac{\partial f}{\partial x} - \frac{\partial v}{\partial z}\frac{\partial f}{\partial y} + \frac{\partial w}{\partial z}\right) + O(\varepsilon^4)}{1 + \varepsilon^2\left[\left(\frac{\partial f}{\partial x}\right)^2 + \left(\frac{\partial f}{\partial y}\right)^2\right]}\right\}|_{z=f} = \frac{\varepsilon^3}{\mathrm{Ca}}\nabla\frac{\nabla f}{\sqrt{1 + \varepsilon^2\left[\left(\frac{\partial f}{\partial x}\right)^2 + \left(\frac{\partial f}{\partial y}\right)^2\right]}}, \tag{14}$$

$$\left(\alpha_t\frac{\partial u}{\partial z} + \beta_t\frac{\partial v}{\partial z}\right)|_{z=f} + \varepsilon^2\left\{\left(\alpha_t\frac{\partial f}{\partial x} + \beta_t\frac{\partial f}{\partial y}\right)\left(-\frac{\partial u}{\partial z}\frac{\partial f}{\partial x} - \frac{\partial v}{\partial z}\frac{\partial f}{\partial y} + 2\frac{\partial w}{\partial z}\right)\right.$$

$$+\alpha_t\left[-2\frac{\partial u}{\partial x}\frac{\partial f}{\partial x}-\left(\frac{\partial u}{\partial y}+\frac{\partial v}{\partial x}\right)\frac{\partial f}{\partial y}+\frac{\partial w}{\partial x}\right]+\beta_t\left[-2\frac{\partial v}{\partial y}\frac{\partial f}{\partial y}-\left(\frac{\partial u}{\partial y}+\frac{\partial v}{\partial x}\right)\frac{\partial f}{\partial x}+\frac{\partial w}{\partial y}\right]\Bigg\}|_{z=f}+O(\varepsilon^4)=0. \tag{15}$$

By neglecting all terms of $O(\varepsilon^2)$ and smaller the above system simplifies considerably and can be averaged over the depth of the film. As in the case of a lubrication approach [8] the depth-averaged form (DAF) derived below can be thought of as a first-order accurate long-wave approximation but with no Reynolds number limitation.

For thin film flows the capillary pressure is of the same order as the fluid pressure; to be consistent with [13, 31, 53] the capillary number is defined as:

$$\mathrm{Ca}=\frac{\varepsilon^3}{6}=\frac{H_0^3}{6L_0^3}, \tag{16}$$

where $L_0=(\sigma H_0/3\rho g\sin\theta)^{1/3}$ represents the associated capillary length-scale; the resulting DAF is therefore valid for the case of small capillary numbers, $\mathrm{Ca}\sim O(\epsilon^3)\ll 1$, only.

Equation (12) results in a balance between the acceleration arising from the pressure and that from gravity, which when integrated with respect to z and applying boundary condition (14), leads to the following familiar equation [13] for pressure:

$$p=-\frac{\varepsilon^3}{\mathrm{Ca}}\nabla^2 f+2\varepsilon\,(f-z)\cot\theta. \tag{17}$$

Integrating the continuity equation (13) using Leibniz's rule and applying boundary conditions (5) and (7) leads to the following depth-averaged equation for the conservation of mass:

$$\int_s^f\left(\frac{\partial u}{\partial x}+\frac{\partial v}{\partial y}+\frac{\partial w}{\partial z}\right)dz=\frac{\partial h}{\partial t}+\frac{\partial\,(h\bar{u})}{\partial x}+\frac{\partial\,(h\bar{v})}{\partial y}=0, \tag{18}$$

where the over-bar denotes the x and y depth-averaged components of velocity, namely:

$$\bar{u}=\frac{1}{h}\int_s^f u dz,\quad \bar{v}=\frac{1}{h}\int_s^f v dz, \tag{19}$$

The DAF of the momentum equations (10) and (11) is obtained in three stages: first the pressure gradient, then the diffusion terms and finally the advection terms are averaged. In the case of the u-momentum equation (10), making use of boundary conditions (5), (7), (15) and equation (13), while noting that fluctuations about the average are zero, in order:

$$\int_s^f\frac{\partial p}{\partial x}dz=h\frac{\partial p}{\partial x}, \tag{20}$$

$$\int_s^f\frac{\partial^2 u}{\partial z^2}dz=\frac{\partial u}{\partial z}|_{z=f}-\frac{\partial u}{\partial z}|_{z=s}=-\frac{\partial u}{\partial z}|_{z=s}, \tag{21}$$

$$\int_s^f\left(\frac{\partial u}{\partial t}+u\frac{\partial u}{\partial x}+v\frac{\partial u}{\partial y}+w\frac{\partial u}{\partial z}\right)dz=\int_s^f\left(\frac{\partial u}{\partial t}+\frac{\partial\,(uu)}{\partial x}+\frac{\partial\,(vu)}{\partial y}+\frac{\partial\,(wu)}{\partial z}\right)dz$$
$$=h\left(\frac{\partial\bar{u}}{\partial t}+\bar{u}\frac{\partial\bar{u}}{\partial x}+\bar{v}\frac{\partial\bar{u}}{\partial y}\right)+\frac{\partial}{\partial x}\int_s^f(\bar{u}-u)^2\,dz+\frac{\partial}{\partial y}\int_s^f(\bar{u}-u)\,(\bar{v}-v)\,dz. \tag{22}$$

The DAF of the v-momentum equation is derived similarly.

After substitution of the pressure equation (17) into the momentum equations and dividing through by the film thickness, the resulting governing system of equations for the unknown averaged velocities $\bar{u}(x,y,t)$, $\bar{v}(x,y,t)$ and the film thickness $h(x,y,t)$ is:

$$\varepsilon\mathrm{Re}\left[\frac{\partial\bar{u}}{\partial t}+\bar{u}\frac{\partial\bar{u}}{\partial x}+\bar{v}\frac{\partial\bar{u}}{\partial y}+\frac{1}{h}\frac{\partial}{\partial x}\int_s^f(\bar{u}-u)^2\,dz+\frac{1}{h}\frac{\partial}{\partial y}\int_s^f(\bar{u}-u)(\bar{v}-v)\,dz\right]$$
$$=\frac{\partial}{\partial x}\left[\frac{\varepsilon^3}{\mathrm{Ca}}\nabla^2(h+s)-2\varepsilon(h+s)\cot\theta\right]-\frac{1}{h}\frac{\partial u}{\partial z}|_{z=s}+2, \tag{23}$$

$$\varepsilon\mathrm{Re}\left[\frac{\partial\bar{v}}{\partial t}+\bar{u}\frac{\partial\bar{v}}{\partial x}+\bar{v}\frac{\partial\bar{v}}{\partial y}+\frac{1}{h}\frac{\partial}{\partial x}\int_s^f(\bar{u}-u)(\bar{v}-v)\,dz+\frac{1}{h}\frac{\partial}{\partial y}\int_s^f(\bar{v}-v)^2\,dz\right]$$
$$=\frac{\partial}{\partial y}\left[\frac{\varepsilon^3}{\mathrm{Ca}}\nabla^2(h+s)-2\varepsilon(h+s)\cot\theta\right]-\frac{1}{h}\frac{\partial v}{\partial z}|_{z=s}, \tag{24}$$

$$\frac{\partial h}{\partial t}+\frac{\partial(h\bar{u})}{\partial x}+\frac{\partial(h\bar{v})}{\partial y}=0. \tag{25}$$

The above system of equations contains four dimensionless parameters: ε, Re, Ca and $\cot\theta$; however, due to the nature of the length-scale L_0 it is possible to avoid one spare parameter - either Ca or ε as per equation (16). Therefore the similarity of the results obtained by solving the DAF depends on two dimensionless groupings only: an inertia parameter $\mathcal{I}=\mathrm{Ca}^{1/3}\cdot\mathrm{Re}$ and gravity parameter $\mathrm{N}=\mathrm{Ca}^{1/3}\cdot\cot\theta$.

The problem is closed in terms of specified averaged inflow conditions and the assumption of fully developed flow both upstream and downstream, namely:

$$\bar{u}|_{x=0}=2/3,\quad \bar{v}|_{x=0}=\frac{\partial\bar{u}}{\partial x}|_{x=l_p}=\frac{\partial\bar{v}}{\partial x}|_{x=l_p}=\frac{\partial\bar{u}}{\partial y}|_{y=0,w_p}=\frac{\partial\bar{v}}{\partial y}|_{y=0,w_p}=0. \tag{26}$$

$$h|_{x=0}=1,\quad \frac{\partial h}{\partial x}|_{x=l_p}=\frac{\partial h}{\partial y}|_{y=0,w_p}=0. \tag{27}$$

2.2 Friction and Dispersion Terms

Equations (23)-((25) contain friction and dispersion terms of the form $\partial_z u|_{z=s}$, $\partial_z v|_{z=s}$ and $\int_s^f(\bar{u}-u)^2\,dz$, $\int_s^f(\bar{v}-v)^2\,dz$, $\int_s^f(\bar{u}-u)(\bar{v}-v)\,dz$, respectively. For the thin film flows of interest, these terms can be determined explicitly by assuming that the velocity profile within the film has the same and consistent self-similar form as the classical Nusselt solution [51], namely:

$$u=3\bar{u}\left(\xi-1/2\xi^2\right),\quad v=3\bar{v}\left(\xi-1/2\xi^2\right), \tag{28}$$

where $\xi=(z-s)/h$.

Note that, proceeding as above is commensurate with the key assumption of the integral-boundary-layer approximation discussed earlier, namely that the velocity profile across the film is parabolic. Although not explored here, various authors suggest alternative ways forward. For the problem of two-dimensional film flow down an incline uniform plane, [35, 36, 37] have proposed the following models: (i) a first-order one which involves approximating the velocity profile using high-order polynomials whose coefficients are determined by gradient expansion of the solution; (ii) a second-order variant which retains terms of second-order-accuracy in the long-wave expansion of the N-S equations and the free-surface stress balance boundary condition, leading to a system of equations for three unknowns - the film thickness, mean flow rate and shear stress at the surface. The latter model has been refined further still [38] by

retaining terms of third-order-accuracy and approximating the velocity profile by polynomials up to eighth-order whose coefficients are obtained by Galerkin projection.

The validity and robustness of using the velocity profiles given by equation (28) in the present work is established in Section 4, even for flow over deep topographic features, by comparison with complementary experimentally measured and numerically predicted freesurface disturbances.

Accordingly, using relations (28) and equation (18) leads to the following analytical expressions for the friction and dispersion terms:

$$\frac{\partial u}{\partial z}|_{z=s} = \frac{3\bar{u}}{h}, \tag{29}$$

$$\frac{\partial v}{\partial z}|_{z=s} = \frac{3\bar{v}}{h}, \tag{30}$$

$$\frac{\partial}{\partial x}\int_s^f (\bar{u}-u)^2\,dz + \frac{\partial}{\partial y}\int_s^f (\bar{u}-u)(\bar{v}-v)\,dz = \frac{1}{5}\left(h\bar{u}\frac{\partial \bar{u}}{\partial x} + h\bar{v}\frac{\partial \bar{u}}{\partial y} - \bar{u}\frac{\partial h}{\partial t}\right), \tag{31}$$

$$\frac{\partial}{\partial x}\int_s^f (\bar{u}-u)(\bar{v}-v)\,dz + \frac{\partial}{\partial y}\int_s^f (\bar{v}-v)^2\,dz = \frac{1}{5}\left(h\bar{u}\frac{\partial \bar{v}}{\partial x} + h\bar{v}\frac{\partial \bar{v}}{\partial y} - \bar{v}\frac{\partial h}{\partial t}\right). \tag{32}$$

Note too, that the above forms for the friction and dispersion terms ensure that the DAF of the governing equations reduces to the familiar lubrication equations [8] when $\mathrm{Re} = 0$.

2.3 Topography Definition

Attention is restricted to flows involving simple, well-defined topography, namely one-dimensional (spanwise) trench, step-up, and step-down features, and in two-dimensions (localised) rectangular trenches. Note, however, that the DAF can be applied to flows over more complex topographies - see for example [54]. Since the topography profile appears as a function in the governing equations, it is not possible to consider completely sharp features. Following previous authors [13, 23, 27], the topography is therefore specified via arctangent functions; for example, a rectangular trench (or peak if desired) is defined as follows:

$$s(x^*,y^*) = \frac{s_0}{4\tan^{-1}\frac{l_t}{2\delta}\tan^{-1}\frac{w_t}{2\delta}}\left[\tan^{-1}\left(\frac{x^*+l_t/2}{\delta}\right) - \tan^{-1}\left(\frac{x^*-l_t/2}{\delta}\right)\right] \times \left[\tan^{-1}\left(\frac{y^*+w_t/2}{\delta}\right) - \tan^{-1}\left(\frac{y^*-w_t/2}{\delta}\right)\right], \tag{33}$$

where $s_0\,(=S_0/H_0)$ is the dimensionless depth ($s_0<0$) or height ($s_0>0$), with $l_t\,(=L_T/L_0)$, $w_t\,(=W_T/L_0)$ and δ the non-dimensional streamwise length, spanwise width and steepness factor, respectively. The coordinate system $(x^*,y^*) = (x-x_t, y-y_t)$ has its origin at the centre of the topography, (x_t,y_t).

3 Method of Solution

3.1 Spatial Discretisation

Equations (23) to (25), incorporating expressions (29) to (32), are solved, subject to boundary conditions (26) and (27), on a rectangular computational domain, $(x,y)\in\Omega = (0,l_p)\times(0,w_p)$, subdivided using a regular spatially staggered mesh arrangement of cells having sides of length Δx and width Δy. The unknown variables, film thickness, h, and the velocity components, $\bar{u}$,

$\bar{v}$, are located at cell centres, (i,j), and cell faces, $(i+1/2,j)$, $(i,j+1/2)$, respectively. The use of a staggered mesh arrangement avoids the well known checkerboard instability [57] that results if central differencing is applied to first-order pressure term derivatives and to the terms in the continuity equation when pressure and velocity components are collocated.

Solving the momentum equations (23) and (24) at cell faces with the convection and time derivative terms grouped together to simply their numerical treatment following the inclusion of the friction and dispersion terms, the continuity equation (25) at cell centres, and omitting for the sake of convenience the overbar denoting velocity averaging, results in the following second-order accurate discretisation scheme:

$$\varepsilon\mathrm{Re}\left(\frac{\partial u}{\partial t}-\frac{u}{5h}\frac{\partial h}{\partial t}+\frac{6}{5}F\left[u\right]\right)|_{i+1/2,j}-\frac{\varepsilon^3}{\mathrm{Ca}}\left(\frac{f_{i+1,j+1}-2f_{i+1,j}+f_{i+1,j-1}-f_{i,j+1}+2f_{i,j}-f_{i,j-1}}{\Delta x\Delta y^2}\right.$$
$$\left.+\frac{f_{i+2,j}-3f_{i+1,j}+3f_{i,j}-f_{i-1,j}}{\Delta x^3}\right)+2\varepsilon\cot\theta\frac{f_{i+1,j}-f_{i,j}}{\Delta x}+\frac{3u_{i+1/2,j}}{h_{i+1/2,j}^2}-2=0, \tag{34}$$

$$\varepsilon\mathrm{Re}\left(\frac{\partial v}{\partial t}-\frac{v}{5h}\frac{\partial h}{\partial t}+\frac{6}{5}F\left[v\right]\right)|_{i,j+1/2}-\frac{\varepsilon^3}{\mathrm{Ca}}\left(\frac{f_{i+1,j+1}-2f_{i,j+1}+f_{i-1,j+1}-f_{i+1,j}+2f_{i,j}-f_{i-1,j}}{\Delta x^2\Delta y}\right.$$
$$\left.+\frac{f_{i,j+2}-3f_{i,j+1}+3f_{i,j}-f_{i,j-1}}{\Delta y^3}\right)+2\varepsilon\cot\theta\frac{f_{i,j+1}-f_{i,j}}{\Delta y}+\frac{3v_{i,j+1/2}}{h_{i,j+1/2}^2}=0, \tag{35}$$

$$\frac{\partial h}{\partial t}|_{i,j}+\frac{h_{i+1/2,j}u_{i+1/2,j}-h_{i-1/2,j}u_{i-1/2,j}}{\Delta x}+\frac{h_{i,j+1/2}v_{i,j+1/2}-h_{i,j-1/2}v_{i,j-1/2}}{\Delta y}=0, \tag{36}$$

where $F\left[\omega\right]=u\partial_x\omega+v\partial_y\omega$ is the convective operator and the following terms are interpolated as shown from neighbouring nodes: $h_{i\pm1/2,j}=\left(h_{i\pm1,j}+h_{i,j}\right)/2$, $h_{i,j\pm1/2}=\left(h_{i,j\pm1}+h_{i,j}\right)/2$.

In the above discrete DAF analogue, as is the case for convection-diffusion problems, proper numerical treatment of the convection terms is very important [55, 56]. The mesh Péclet number, Pe, stability condition (see [57], for example), defined as the ratio of the convection to friction term in the momentum equation, is given by:

$$\mathrm{Pe}=\frac{2\varepsilon\mathrm{Re}h^2\max\left(u,v\right)}{5\min\left(\Delta x,\Delta y\right)}\leq 2\Rightarrow\mathrm{Re}\leq\mathrm{Re}_{cr}=\frac{15\min\left(\Delta x,\Delta y\right)}{2\varepsilon}. \tag{37}$$

For typical mesh spacings of $\Delta x=\Delta y=0.05$ and with $\varepsilon=0.1$ the value of the critical Reynolds number, Re_{cr}, is small and equal to 3.75, illustrating the restrictiveness of this constraint apropos the accurate solution of the thin film flows of interest.

To alleviate this restriction the convective operator $F\left[\omega\right]$ is discretized using a second-order accurate total variation diminishing (TVD) scheme [58]. As such, the first term of the convective operator, $u\partial_x\omega$, at a general point (i,j) takes the form:

$$\frac{\partial\omega}{\partial x}|_{i,j}=\frac{u_{i,j}^{+}}{4\Delta x}\left\{\left(\omega_{i,j}-\omega_{i-1,j}\right)\left[2+\psi\left(\frac{\omega_{i+1,j}-\omega_{i,j}}{\omega_{i,j}-\omega_{i-1,j}}\right)\right]-\left(\omega_{i-1,j}-\omega_{i-2,j}\right)\psi\left(\frac{\omega_{i,j}-\omega_{i-1,j}}{\omega_{i-1,j}-\omega_{i-2,j}}\right)\right\}$$
$$+\frac{u_{i,j}^{-}}{4\Delta x}\left\{\left(\omega_{i+1,j}-\omega_{i,j}\right)\left[2+\psi\left(\frac{\omega_{i,j}-\omega_{i-1,j}}{\omega_{i+1,j}-\omega_{i,j}}\right)\right]-\left(\omega_{i+2,j}-\omega_{i+1,j}\right)\psi\left(\frac{\omega_{i+1,j}-\omega_{i,j}}{\omega_{i+2,j}-\omega_{i+1,j}}\right)\right\}, \tag{38}$$

where $u_{i,j}^{+}=u_{i,j}+|u_{i,j}|$, $u_{i,j}^{-}=u_{i,j}-|u_{i,j}|$, and $\psi\left(\eta\right)=\left(\eta^2+\eta\right)/\left(\eta^2+1\right)$ is the well known van Albada flux limiter [57]; the second term, $v\partial_y\omega$, in $F\left[\omega\right]$ is expressed similarly. The formulation is easily shifted to the appropriate staggered grid location to obtain $F\left[u\right]_{i+1/2,j}$ or $F\left[v\right]_{i,j+1/2}$ and the following terms can be interpolated from neighbouring nodes:

$$u_{i,j+1/2} = \left(u_{i-1/2,j}+u_{i+1/2,j}+u_{i-1/2,j+1}+u_{i+1/2,j+1}\right)/4, \tag{39}$$
$$v_{i+1/2,j} = \left(v_{i,j-1/2}+v_{i,j+1/2}+v_{i+1,j-1/2}+v_{i+1,j+1/2}\right)/4. \tag{40}$$

To simplify the description of the calculation procedure presented below, it is convenient to separate the leading temporal u, v and h terms from the discretized u-momentum, v-momentum and continuity operators and to express them as functions $\mathcal{M}^u_{i+1/2,j}$, $\mathcal{M}^v_{i,j+1/2}$ and $\mathcal{M}^h_{i,j}$, respectively. This enables equations (34)-(36) to be rewritten as:

$$\varepsilon \mathrm{Re} \frac{\partial u}{\partial t}|_{i+1/2,j} + \mathcal{M}^u_{i+1/2,j}(u,v,h) = 0, \quad (41)$$

$$\varepsilon \mathrm{Re} \frac{\partial v}{\partial t}|_{i,j+1/2} + \mathcal{M}^v_{i,j+1/2}(u,v,h) = 0, \quad (42)$$

$$\frac{\partial h}{\partial t}|_{i,j} + \mathcal{M}^h_{i,j}(u,v,h) = 0, \quad (43)$$

The discrete form of the $\frac{\partial h}{\partial t}$ term, which appears in $\mathcal{M}^u$ and $\mathcal{M}^v$, of equations (34) and (35), is obtained at the appropriate staggered mesh location via equation (43). The locations of the independent variables (u, v, h), when determining the functions $\mathcal{M}^u_{i+1/2,j}$, $\mathcal{M}^v_{i,j+1/2}$ and $\mathcal{M}^h_{i,j}$ are shown in Fig. 2.

Clearly, when $\mathrm{Re} = 0$ the solution procedure simplifies considerably since the terms containing time derivatives on the left hand side of the momentum equations (41) and (42) disappear.

3.2 Temporal Discretisation

The automatic adaptive time-stepping procedure adopted employs an estimate of the local truncation error (LTE) obtained from the difference between an explicit predictor stage and the current solution stage to optimise the size of time steps and minimise computational waste.

Fully explicit, second order accurate in time discretisations of equations (41) - (43) can be used to predict (pr) values for u, v and h, as follows:

$$u_{\mathrm{pr}}|^{n+1}_{i+1/2,j} = \gamma^2 u^{n-1}_{i+1/2,j} + \left(1-\gamma^2\right) u^n_{i+1/2,j} - \frac{\Delta t^{n+1}}{\varepsilon \mathrm{Re}} (1+\gamma) \mathcal{M}^u_{i+1/2,j}(u^n, v^n, h^n), \quad (44)$$

$$v_{\mathrm{pr}}|^{n+1}_{i,j+1/2} = \gamma^2 v^{n-1}_{i,j+1/2} + \left(1-\gamma^2\right) v^n_{i,j+1/2} - \frac{\Delta t^{n+1}}{\varepsilon \mathrm{Re}} (1+\gamma) \mathcal{M}^v_{i,j+1/2}(u^n, v^n, h^n), \quad (45)$$

$$h_{\mathrm{pr}}|^{n+1}_{i,j} = \gamma^2 h^{n-1}_{i,j} + \left(1-\gamma^2\right) h^n_{i,j} - \Delta t^{n+1} (1+\gamma) \mathcal{M}^h_{i,j}(u^n, v^n, h^n), \quad (46)$$

where n and $n+1$ denote values at the end of the nth and $(n+1)$st time steps, $t = t^n$ and $t = t^{n+1}$ respectively, and $\gamma = \Delta t^{n+1}/\Delta t^n = (t^{n+1} - t^n)/(t^n - t^{n-1})$.

Adaptive time-stepping is performed by keeping the LTE for u_{pr} within a specified tolerance that in practice automatically restricts the LTE for v_{pr} and h_{pr} and provides a means of increasing the time step in a controlled manner. The LTE for u_{pr} at the predictor stage can be expressed via a Taylor series expansion of equation (44) in the form:

$$(\mathrm{LTE})_{\mathrm{pr}}|_{i+1/2,j} = \frac{(\Delta t^{n+1})\Delta t^n (1+\gamma)}{6} \frac{\partial^3 u}{\partial t^3}|_{i+1/2,j,t=t_p}, \quad (47)$$

with the third-order time derivative term evaluated at time $t_p \in (t^n, t^{n+1})$.

In the present work, an implicit β-method [58] is used to advance the solution in time:

$$\begin{aligned} u^{n+1}_{i+1/2,j} &+ \frac{\beta\Delta t^{n+1}}{\varepsilon\mathrm{Re}}\mathcal{M}^u_{i+1/2,j}\left(u^{n+1},v^{n+1},h^{n+1}\right) \\ &= u^n_{i+1/2,j} + \frac{(\beta-1)\,\Delta t^{n+1}}{\varepsilon\mathrm{Re}}\mathcal{M}^u_{i+1/2,j}\left(u^n,v^n,h^n\right), \qquad (48) \\ v^{n+1}_{i,j+1/2} &+ \frac{\beta\Delta t^{n+1}}{\varepsilon\mathrm{Re}}\mathcal{M}^v_{i,j+1/2}\left(u^{n+1},v^{n+1},h^{n+1}\right) \\ &= v^n_{i,j+1/2} + \frac{(\beta-1)\,\Delta t^{n+1}}{\varepsilon\mathrm{Re}}\mathcal{M}^v_{i,j+1/2}\left(u^n,v^n,h^n\right), \qquad (49) \\ h^{n+1}_{i,j} &+ \beta\Delta t^{n+1}\mathcal{M}^h_{i,j}\left(u^{n+1},v^{n+1},h^{n+1}\right) \\ &= h^n_{i,j} + (\beta-1)\,\Delta t^{n+1}\mathcal{M}^h_{i,j}\left(u^n,v^n,h^n\right). \qquad (50) \end{aligned}$$

Note that for $\beta = 1/2$ the method reduces to the second order accurate in time, but conditionally stable Crank-Nicolson scheme, whereas $\beta = 1$ leads to the fully implicit first order accurate in time unconditionally stable Laasonen method.

The LTE for u at the solution (sol) stage is similarly given by a Taylor series expansion of equation (48):

$$(\mathrm{LTE})_{\mathrm{sol}}|_{i+1/2,j} = -\frac{(\Delta t^{n+1})^3}{12}\frac{\partial^3 u}{\partial t^3}|_{i+1/2,j,t=t_s}, \quad t_s \in (t^n, t^{n+1}). \qquad (51)$$

As described in [59], the assumption that the third order derivative term varies by only a small amount over the time step enables the LTE to be estimated as:

$$(\mathrm{LTE})_{i+1/2,j} = \frac{u^{n+1}_{i+1/2,j} - u_{\mathrm{pr}}|^{n+1}_{i+1/2,j}}{1+2[(1+\gamma)/\gamma]}, \qquad (52)$$

which, following [60], is used to obtain an estimate of the overall truncation error by finding its Euclidean norm that, in turn, is used to specify the next time step Δt^{n+2} via:

$$\Delta t^{n+2} = 0.9\Delta t^{n+1}\left(\frac{\mathrm{TOL}}{||\mathrm{LTE}||}\right)^{1/3}, \qquad (53)$$

if $||\mathrm{LTE}|| \leq \mathrm{TOL}$. The iteration is restarted with half the current time step if $||\mathrm{LTE}|| > \mathrm{TOL}$, where TOL is a user prescribed tolerance.

3.3 Multigrid Solver

At the solution stage of the temporal discretisation, the system of the equations (48) to (50) is solved using a multigrid formulation that enables a system with N unknowns to be solved in only $O\,(\mathrm{N})$ operations. The basis of this approach, as described in several comprehensive texts – see for example [57], exploits the convergence rates of iterative solvers, such as Gauss-Seidel or Jacobi smoothers, to effectively reduce local (high-frequency) errors present in the solution on a particular computational grid, while global (low-frequency) errors are reduced by employing a hierarchy of successively finer grids, $G^0, \ldots, G^k, \ldots, G^K$, where G^0 denotes the coarsest and G^K the finest grid level.

For a specified number of cells on the coarsest grid G^0, n^0_x and n^0_y in the x and y directions respectively, the number of cells on an arbitrary grid G^k say, is $n^k_x = n^0_x 2^k$, $n^k_y = n^0_y 2^k$. This results in grid spacings on G^k of $\Delta x^k = l_p/n^k_x = \Delta x^0 2^{-k}$, $\Delta y^k = w_p/n^k_y = \Delta y^0 2^{-k}$, where $\Delta x^0 = l_p/n^0_x$ and $\Delta y^0 = w_p/n^0_y$ are the grid spacings on G^0.

To simplify the explanation and the steps taken in the multigrid process, the system of discrete equations (48) to (50) is rewritten in the following way:

$$\mathcal{N}^u_{i+1/2,j}\left(u^{n+1},v^{n+1},h^{n+1}\right)=\mathcal{F}^u_{i+1/2,j}\left(u^n,v^n,h^n\right), \tag{54}$$

$$\mathcal{N}^v_{i,j+1/2}\left(u^{n+1},v^{n+1},h^{n+1}\right)=\mathcal{F}^v_{i,j+1/2}\left(u^n,v^n,h^n\right), \tag{55}$$

$$\mathcal{N}^h_{i,j}\left(u^{n+1},v^{n+1},h^{n+1}\right)=\mathcal{F}^h_{i,j}\left(u^n,v^n,h^n\right), \tag{56}$$

where $\mathcal{N}^u_{i+1/2,j}$, $\mathcal{N}^v_{i,j+1/2}$ and $\mathcal{N}^h_{i,j}$ are the time-dependent nonlinear operators and $\mathcal{F}^u_{i+1/2,j}$, $\mathcal{F}^v_{i,j+1/2}$ and $\mathcal{F}^h_{i,j}$ are the right-hand side functions that are defined by the solution on the previous time step.

In the present work a combined full approximation storage (FAS) and full multigrid (FMG) technique is employed. The latter is based on the fact that an initial guess (Gs) for the multigrid solver on each grid $G^k \in \left[G^1, G^K\right]$ is provided by FMG interpolation of the solution (Sl) from the coarser grid G^{k-1} (see Fig. 3) using bilinear interpolation operators on a staggered grid system $I^u_{k-1\to k}, I^v_{k-1\to k}, I^h_{k-1\to k}$ (see Appendix A):

$$u^{\mathrm{Gs}}_k = I^u_{k-1\to k}\left(u^{\mathrm{Sl}}_{k-1}\right), \quad v^{\mathrm{Gs}}_k = I^u_{k-1\to k}\left(v^{\mathrm{Sl}}_{k-1}\right), \quad h^{\mathrm{Gs}}_k = I^h_{k-1\to k}\left(h^{\mathrm{Sl}}_{k-1}\right), \tag{57}$$

where, for the sake of simplicity, the coordinate and time indices have been omitted.

The solution process consists of performing a fixed number of FAS V-cycles on intermediate grid levels $G^k \in [G^1, G^{K-1}]$ (usually 1 to 3 V-cycles) and up to 10 V-cycles on the finest grid level G^K (that is, sufficient V-cycles are executed until the residuals have been reduced to a specified tolerance). The structure of a single FAS multigrid V-cycle on an arbitrary grid level G^k may be described in the same pseudo-code formalism as in [12]:

$$\left(u^{\mathrm{Sl}}_k, v^{\mathrm{Sl}}_k, h^{\mathrm{Sl}}_k\right) = \mathrm{FASCYC}\left(k, u^{\mathrm{Gs}}_k, v^{\mathrm{Gs}}_k, h^{\mathrm{Gs}}_k, \mathcal{F}^u_k, \mathcal{F}^v_k, \mathcal{F}^h_k, \nu_{\mathrm{pre}}, \nu_{\mathrm{post}}\right), \tag{58}$$

where ν_{pre} and ν_{post} are number of pre- and post-relaxations of the multigrid cycle (usually $\nu_{\mathrm{pre}} = \nu_{\mathrm{post}} = 2$).

1. Pre-smoothing stage

- Apply the relaxation scheme (see next subsection) ν_{pre} times to obtain first corrected appproximation (Rl):

$$\left(u^{\mathrm{Rl}}_k, v^{\mathrm{Rl}}_k, h^{\mathrm{Rl}}_k\right) = \mathrm{RELAX}^{\nu_{\mathrm{pre}}}\left(u^{\mathrm{Gs}}_k, v^{\mathrm{Gs}}_k, h^{\mathrm{Gs}}_k, \mathcal{F}^u_k, \mathcal{F}^v_k, \mathcal{F}^h_k\right), \tag{59}$$

2. Coarse-grid correction stage

- Compute the defects:

$$d^u_k = \mathcal{F}^u_k - \mathcal{N}^u_k\left(u^{\mathrm{Rl}}_k, v^{\mathrm{Rl}}_k, h^{\mathrm{Rl}}_k\right), \quad d^v_k = \mathcal{F}^v_k - \mathcal{N}^v_k\left(u^{\mathrm{Rl}}_k, v^{\mathrm{Rl}}_k, h^{\mathrm{Rl}}_k\right), \quad d^h_k = \mathcal{F}^h_k - \mathcal{N}^h_k\left(u^{\mathrm{Rl}}_k, v^{\mathrm{Rl}}_k, h^{\mathrm{Rl}}_k\right), \tag{60}$$

- Restrict the defects to the next coarser grid level using full-weighting restriction operators for staggered grids $R^u_{k\to k-1}, R^v_{k\to k-1}, R^h_{k\to k-1}$ (see Appendix A):

$$d^u_{k-1} = R^u_{k\to k-1}\left(d^u_k\right), \quad d^v_{k-1} = R^v_{k\to k-1}\left(d^v_k\right), \quad d^h_{k-1} = R^h_{k\to k-1}\left(d^h_k\right), \tag{61}$$

- Restrict the solution to get the initial guess for the next coarser grid level:

$$u^{\mathrm{Gs}}_{k-1} = R^u_{k\to k-1}\left(u^{\mathrm{Rl}}_k\right), \quad v^{\mathrm{Gs}}_{k-1} = R^v_{k\to k-1}\left(v^{\mathrm{Rl}}_k\right), \quad h^{\mathrm{Gs}}_{k-1} = R^h_{k\to k-1}\left(h^{\mathrm{Rl}}_k\right), \tag{62}$$

- Compute the right-hand side on the next coarser grid level:

$$\mathcal{F}^u_{k-1} = d^u_{k-1} + \mathcal{N}^u_{k-1}\left(u^{\mathrm{Gs}}_{k-1}, v^{\mathrm{Gs}}_{k-1}, h^{\mathrm{Gs}}_{k-1}\right), \quad \mathcal{F}^v_{k-1} = d^v_{k-1} + \mathcal{N}^v_{k-1}\left(u^{\mathrm{Gs}}_{k-1}, v^{\mathrm{Gs}}_{k-1}, h^{\mathrm{Gs}}_{k-1}\right),$$

$$\mathcal{F}^h_{k-1} = d^h_{k-1} + \mathcal{N}^h_{k-1}\left(u^{\mathrm{Gs}}_{k-1}, v^{\mathrm{Gs}}_{k-1}, h^{\mathrm{Gs}}_{k-1}\right), \tag{63}$$

  If $k = 0$ a coarsest grid solver is employed (equations (54) to (56) can be solved directly or, as is the case here, using relaxation – see section 3.4). If $k > 0$ the FAS cycle is used to update the next $k-1$ coarser grid solution:

$$\left(u^{\mathrm{Sl}}_{k-1}, v^{\mathrm{Sl}}_{k-1}, h^{\mathrm{Sl}}_{k-1}\right) = \mathrm{FASCYC}\left(k-1, u^{\mathrm{Gs}}_{k-1}, v^{\mathrm{Gs}}_{k-1}, h^{\mathrm{Gs}}_{k-1}, \mathcal{F}^u_{k-1}, \mathcal{F}^v_{k-1}, \mathcal{F}^h_{k-1}, \nu_{\mathrm{pre}}, \nu_{\mathrm{post}}\right), \tag{64}$$

- Compute the corrections:

$$e^u_{k-1} = u^{\mathrm{Sl}}_{k-1} - u^{\mathrm{Gs}}_{k-1}, \quad e^v_{k-1} = v^{\mathrm{Sl}}_{k-1} - v^{\mathrm{Gs}}_{k-1}, \quad e^h_{k-1} = h^{\mathrm{Sl}}_{k-1} - h^{\mathrm{Gs}}_{k-1}, \tag{65}$$

- Interpolate the corrections on the fine grid level using bilinear interpolation operators for staggered grids $I^u_{k-1\to k}, I^v_{k-1\to k}, I^h_{k-1\to k}$ (see Appendix A):

$$e^u_k = I^u_{k-1\to k}\left(e^u_{k-1}\right), \quad e^v_k = I^v_{k-1\to k}\left(e^v_{k-1}\right), \quad e^h_k = I^h_{k-1\to k}\left(e^h_{k-1}\right), \tag{66}$$

- Compute the second corrected approximation (Cr):

$$u^{\mathrm{Cr}}_k = u^{\mathrm{Rl}}_k + e^u_k, \quad v^{\mathrm{Cr}}_k = v^{\mathrm{Rl}}_k + e^v_k, \quad h^{\mathrm{Cr}}_k = h^{\mathrm{Rl}}_k + e^h_k, \tag{67}$$

3. Post-smoothing stage

- Apply the relaxation scheme ν_{post} times to get the final solution (Sl):

$$\left(u^{\mathrm{Sl}}_k, v^{\mathrm{Sl}}_k, h^{\mathrm{Sl}}_k\right) = \mathrm{RELAX}^{\nu_{\mathrm{post}}}\left(u^{\mathrm{Cr}}_k, v^{\mathrm{Cr}}_k, h^{\mathrm{Cr}}_k, \mathcal{F}^u_k, \mathcal{F}^v_k, \mathcal{F}^h_k\right). \tag{68}$$

3.4 Relaxation Methodology

Due to the staggered nature of the discretisation involved, the relaxation methodology employs a lexicographic box smoothing Gauss-Seidel scheme [57] to define a collective local relaxation which encompasses the associated variables u, v and h; this efficiently retains the diagonal dominance of the relaxation scheme. The set of algebraic equations (54) to (56) is written in a linearised form using the Newton-Raphson method. For each cell, see Fig. 2, five coupled equations (two each from the u-momentum and v-momentum equations and one from the continuity equation, given in Appendix B) are solved for the unknown increments $\Delta u_{i+1/2,j}$, $\Delta u_{i-1/2,j}$, $\Delta v_{i,j+1/2}$, $\Delta v_{i,j-1/2}$, $\Delta h_{i,j}$ with the new approximations given by:

$$\begin{aligned}
\tilde{u}_{i+1/2,j} &= u_{i+1/2,j} + \Delta u_{i+1/2,j}, \\
\tilde{u}_{i-1/2,j} &= u_{i-1/2,j} + \Delta u_{i-1/2,j}, \\
\tilde{v}_{i,j+1/2} &= v_{i,j+1/2} + \Delta v_{i,j+1/2}, \\
\tilde{v}_{i,j-1/2} &= v_{i,j-1/2} + \Delta v_{i,j-1/2}, \\
\tilde{h}_{i,j} &= h_{i,j} + \Delta h_{i,j},
\end{aligned} \tag{69}$$

updated simultaneously; and where each velocity component is updated twice, while the film thickness is updated only once per relaxation sweep. Dirichlet boundary conditions are assigned as exact values at the boundary points, whereas Neumann boundary conditions are implemented by employing ghost nodes at the edge of the computational domain.

4 Results

All of the solutions generated were obtained using the implicit time-stepping scheme described above, with $\beta = 3/4$, starting with the initial condition of a flat free-surface ($h = 1 - s$) and velocity profile $u = \frac{2}{3}h^2$, $v = 0$ (commensurate with Re = 0). A computational domain with $l_p = w_p = 100$, was chosen, large enough to ensure fully developed flow both upstream and downstream of the topography and of sufficient extent to negate edge effects. The coarsest multigrid level G^0 had $n_x^0 = n_y^0 = 64$ ($n_x^0 = 64$ in one-dimension) and a finest grid level G^4 had $n_x^4 = n_y^4 = 1024$ (G^5 with $n_x^5 = 2048$ in one-dimension) uniformly spaced cells. At each time step sufficient multigrid V-cycles are performed to reduce residuals on the finest mesh level to below 10^{-6}. A typical value of the time adaptive tolerance used in the computations is TOL $\approx 10^{-3}$. The choice of steepness parameter, δ, is also important in ensuring the mesh independence of solutions; for all the topography types considered (one-dimensional trench, step-up, step-down and two-dimensional trench), the results obtained were found to be independent of δ provided $\delta \leq \delta_{cr} = 10^{-3}$.

In order to facilitate direct comparison with experiment [31], the focus of the ensuing investigation is that of gravity-driven flow of thin water films with fixed fluid properties $\rho = 1000\text{kg} \cdot \text{m}^{-3}$, $\mu = 0.001\text{Pa} \cdot \text{s}$ and $\sigma = 0.07\text{N} \cdot \text{m}^{-1}$. As such, θ is taken to be 30° unless stated otherwise, with spanwise topography located with its centre at $x_t = 50$ and localised topography shifted upstream slightly and centred on $(x_t, y_t) = (30.77, 50)$. Consequently, for specified values of θ and Re the other parameters appearing in the calculation can be easily derived in terms of them and the fixed fluid properties; for example, H_0 and Ca, can be written as:

$$H_0 = \left(\frac{2\mu^2}{\rho^2 g_0}\right)^{1/3} \left(\frac{\text{Re}}{\sin\theta}\right)^{1/3}, \quad \text{Ca} = \left(\frac{g_0\mu^4}{2\rho\sigma^3}\right)^{1/3} \left(\text{Re}^2 \sin\theta\right)^{1/3}. \tag{70}$$

Two detailed sets of results are presented; Table 1 summarises the range of flow parameters investigated and how, for fixed fluid properties, the non-dimensional groupings involved change in concert. Accordingly, other than for simple step-up and step-down spanwise features, it is convenient to utilise a coordinate system scaled by the fixed streamwise dimension of the topography, namely $(x^o, y^o) = (x^*, y^*)/l_t$; in all cases the planar incline containing the topography and free-surface location is scaled with respect to the fixed height/depth of the topography, namely $s^* = s/s_0$ and $f^* = (f-1)/s_0$, respectively.

Before investigating the flows in detail it is useful to comment on the efficiency of the chosen method of solution, in particular since the equation set involved is hyperbolic in nature. Fig. 4 shows how the CPU time for a typical time step depends on the grid density - the problem used as a benchmark is that of three-dimensional flow over a square, trench topography as considered later in Section 4.2, for the same flow parameters. The slope of the quasi-linear plots in Fig. 4, for both values of Re which differ by an order of magnitude, show that a solution efficiency of O(N), where N is the number of unknowns, is achieved by the multigrid strategy adopted.

4.1 Thin film flow over spanwise topography

The accuracy of the DAF for predicting two-dimensional flow over spanwise topography is quantified by comparison with experimental data [31] and accurate finite element solutions of the full N-S problem - see [61] for a description of the methodology involved. Fig. 5 reveals the effect of Re on the streamwise free-surface profile for the flow of a thin water film over a trench topography of width L_t =1.2 mm and depth $S_0 = 20\mu$m. Figs. 5(a) and (b) show the evolution of the solution towards steady-state for (a) Re = 5 and (b) Re = 15. Such solutions are obtained in a matter of minutes, with higher Reynolds number flows taking longer to reach

steady-state due to the increased inherent non-linearity. Fig. 5(c) demonstrates the influence of inertia on the free-surface profile, showing predictions for the cases Re = 5, 15 and 30, corresponding to $H_0 = 126.8$, 182.9 and 230.5 μm, respectively. They reveal that increasing Re leads to amplification and widening of both the capillary ridge and the free-surface depression over the trench. Note also the exacerbated free-surface disturbance upstream of the capillary ridge with increasing Re.

Fig. 6 compares steady-state free-surface profiles obtained using the DAF and corresponding FE solutions for the experimental cases considered by Decre & Baret [31]. Figs. 6(a) and 6(b) consider flow of a thin water film, with Re = 2.45, over spanwise step-up and step-down topographies respectively of depth/height $|s_0| = 0.2$, while Fig. 6(c) considers flow with Re = 2.84 over a spanwise trench of depth $s_0 = 0.19$ and width l_t=1.51. In all three cases, the DAF and FE predictions are indistinguishable from each other, while the agreement with their experimentally measured counterparts is excellent as exemplified in the blown-up insert of Fig. 6(c) showing the free-surface shape across and upstream of the capillary ridge. Indeed the r.m.s. error between the predicted DAF and experimentally obtained free-surface profiles is approximately 1.5% for all three spanwise topographies, which lies well within the reported experimental accuracy of 2% [31].

A wider range of parameter space is now considered by retaining the same fluid properties as used by [31], i.e. those of water, while changing Re - see Table 1. Figs. 7 and 8 show the effect of increasing inertia and/or topography amplitude on the free surface profiles for flow over step-up and step-down topography, respectively, for cases with Re = 15 and Re = 30 and $|s_0| = 0.2$ and $|s_0| = 1.0$. The corresponding predictions from lubrication theory [14] are also given for comparison purposes. These figures show that increasing inertia results in a widening and amplification of the free-surface disturbance, leading to larger free-surface depressions and capillary ridges upstream of the step-up and step-down topography respectively. It is evident that: (i) the DAF and FE predictions are in close agreement; (ii) lubrication theory, although capturing the essential features, significantly under predicts the associated capillary ridges and depressions; (iii) the discrepancy between the lubrication predictions and the DAF and FE ones is exacerbated by increasing either Re or $|s_0|$.

These findings are quantified in greater detail in Figs. 9(a)-(d), which show contour plots of the discrepancy between lubrication [14] and DAF predictions and corresponding FE solutions of the full N-S equations. Following [13], the error is quantified by the maximum percentage discrepancy between the lubrication or DAF predictions, measured normal to the N-S profile. This measure is preferred to a r.m.s. error since the latter would be unduly biased by the extensive asymptotic flow regions where all free-surface profiles are indistinguishable. Note that the maximum error occurs close to the peak of the topography, over the steeply sloping section of the free-surface, whereas the predicted errors in the vicinity of the free-surface depression (step-up) and capillary ridge (step-down) are typically much less [13].

For both sets of contours, the discrepancies associated with the step-down flow become larger once the values of Re and $|s_0|$ become significant. The errors in the lubrication predictions are consistently greater than those obtained with the DAF, being typically 3 times and 1.5 times larger for the step-up and step-down cases, respectively. For example, for the extreme step-up case with Re = 30 and $|s_0| = 1.0$, the DAF error is only 5.5% compared to lubrication theory's 16%, while for a step-down these errors are 12% and 22% respectively.

Although different in magnitude, the upper two discrepancy contours have roughly the same shape suggesting that the source of error for both step-up and step-down configurations is predominately one of the neglect of inertia, consistent with the basis of lubrication theory. The lower discrepancy contours paint a different picture; the step-up ones being much steeper but lower in magnitude than the step-down ones (which are consistent in shape and form,

though not magnitude, with their lubrication counterpart) suggesting that for the former the relative step height is the more dominate cause of discrepancy.

The source of the greater discrepancy associated with the stepdown can be traced to the underlying flow structure as Re and $|s_0|$ are increased. Under Stokes flow, Re = 0, conditions the eddy structure associated with an equivalent step-up and step-down would be mirror images of each other. Figs. 10 and 11 show that increasing Re reduces (enlarges) the lateral and vertical extent of the corner eddy which is present in the case of a step-up (step-down); as can be seen, the effect becomes more pronounced the larger the value of $|s_0|$. Accordingly, it is arguably the neglect of vertical velocity terms of $O(\varepsilon^2)$ and the use of the classical Nusselt solution in determining the friction and dispersion terms in regions of the flow where a large eddy exists, as a consequence of the nature of the topography present [61], that leads to a greater discrepancy. That said, except at the extreme values of Re and $|s_0|$ over the range considered, the free-surface profiles obtained with the DAF and from FE solutions of the full N-S equations are comparable and encouragingly good.

Taking the finite element solution of the full N-S as the benchmark, the relative difference in the magnitude of the error associated with the corresponding solutions obtained with the DAF and lubrication equations is shown more concisely in Figs. 9(e) and (f) as contours of the ratio of the latter to the former. For the step-up topography, Fig. 9(e) shows that for fixed $|s_0|$, the relative error increases substantially as Re increases but that increasing $|s_0|$ for a fixed value of Re the effect is less dramatic. For the step-down topography, Fig. 9(f) reveals that the dependence on $|s_0|$ and Re is more subtle and, for example, increasing $|s_0|$ for a fixed Re can reduce the ratio of the errors significantly.

4.2 Thin film flow over localised topography

The DAF is now used to predict the effect of inertia on three-dimensional thin film flow over localised (two-dimensional) topography based on the square trench used by [31] with $L_t = W_t = 1.2mm$ and $|S_0| = 25\mu m$. For a topography of this depth and the Re range considered, see Table 1, according to Fig. 9 it is not unreasonable to expect the maximum discrepancy in the predicted free-surface profiles to be of the order of 1% only (since $|s_0| = 0.197$ and 0.092 for Re = 5 and 50, respectively).

Fig. 12 shows the effect of Re on the three-dimensional free-surface disturbance caused by this square trench. Each case exhibits a characteristic 'horseshoe'-shaped 'bow-wave', free-surface depression over the trench, a downstream peak or 'surge' caused by the fact that, for three-dimensional flow, liquid exits the trench across a narrower length than across which it enters [13], and 'comet-tail'. Note that no such 'surge' mechanism exists for two-dimensional flow over a completely spanwise trench, which explains the lack of a downstream surge in the profiles given in Figs. 5(c) and 6(c). Increasing inertia causes a gradual rise in and widening of the free surface disturbance and reduction in the extent of the 'comet-tail'. These effects are seen more clearly in Fig. 13 which gives the corresponding streamwise and spanwise free-surface profiles through the centre of the topography. Fig. 13(a) shows that increasing Re from 5 to 50 more than doubles the magnitude of the capillary ridge ($f^* = 0.015$ compared with $f^* = 0.037$) and roughly trebles the size of the downstream surge ($f^* = 0.023$ compared to $f^* = 0.067$).

The effect of inertia on the downstream surge can be explored in more detail as follows. For small Re, fluid enters the trench across its upstream side and both spanwise sides due to lateral pressure gradients resulting from the spanwise curvature of the free-surface. Since the flow is steady, fluid entering the trench must leave it on the downstream side. As the Re is increased the downstream surge becomes more focused; by the time Re = 50 it creates a free-surface disturbance larger than that of the downstream capillary ridge, Fig. 13(a); in addition it is

positioned further upstream. A plausible explanation for what is observed is that increasing inertia gradually overcomes the lateral pressure gradients causing the flow to become essentially streamwise; in which case fluid enters and exits the trench topography principally across its upstream and downstream sides respectively, and only fractionally if at all via its spanwise sides.

Figs. 14 and 15 analyse how inertia affects the transition to two-dimensional, spanwise flow as the trench width in the spanwise direction, W_t, is increased for fixed L_t=1.2mm. The free-surface profiles given in Fig. 14, viewed from the downstream side, show that increasing trench aspect ratio $A = W_t/L_t$, causes the bow wave to broaden while increasing Re leads to larger free-surface disturbances that are more sharply focussed around the streamwise centreline. For the cases shown, increasing A from 5 to 10 causes the downstream surge to bifurcate into two smaller ones lying either side of the streamwise centreline. The progression to two-dimensional flow can be seen more clearly by the streamwise and spanwise free-surface profiles shown in Fig. 15 for Re = 5 and 50 and trench aspect ratio A = 1, 5, 10 and ∞ (i.e. spanwise topography). Increasing A from 1 to 5 has a dramatic effect on the free surface depression and on the upstream capillary ridge, while for $A = 10$ the streamwise profiles have much reduced downstream surges. The sharper focus of the Re = 50 flow around the streamwise centreline is shown by the spanwise free-surface profiles in Fig. 15(d) and by the fact that a larger aspect ratio is needed for its streamwise profile to approximate that of the two-dimensional case shown in Fig. 5. This is reinforced by calculating the difference in the streamwise free-surface profiles obtained for finite A and the case $A \to \infty$ in the same way as the discrepancy contours of Fig. 9 were generated. For Re = 5, these are found to be 0.74% and 0.24% for $A = 5$ and $A = 10$, respectively; whereas for Re = 50 they are 0.97% and 0.31%, respectively. This behaviour can be explained in physical terms by noting that the Re = 50 case has larger streamwise inertia and therefore will have less of a tendency than the Re = 5 case to spread across a given trench geometry.

The final two figures consider the competing effects of inertia and the normal component of gravity on the free-surface disturbance induced by the square trench topography considered above. The parameter measuring the relative importance of the normal component of gravity is $\mathrm{N} = \mathrm{Ca}^{1/3} \cot\theta$; since the fluid properties are fixed, the influence of N is explored via changes to the inclination angle θ of the planar surface - see Table 1. Fig. 16 shows how decreasing θ (increasing N) suppresses all free-surface disturbances, reducing considerably the magnitude of the bow wave, downstream surge and free-surface depression over the trench. The streamwise and spanwise free-surface profiles given in Fig. 17 show more clearly that the bow wave migrates upstream as θ decreases while the downstream surge is more resistant to changes in θ and its location remains effectively constant.

5 Conclusions

Gravity-driven thin film flow over various spanwise and local topographical features is explored to ascertain the influence of inertia, via the numerical solution of a model system of coupled equations formed by depth-averaging the governing general N-S and continuity equations. The velocity profile within the film is assumed to have the same self-similar form as the classical Nusselt solution in order to close the problem. The solution strategy purposely developed to generate accurate mesh independent solutions to their discrete analogue employs multigridding, error-controlled automatic adaptive time-stepping, a staggered mesh arrangement for the dependent variables and proper treatment of the nonlinear convective terms via a second order accurate TVD scheme in conjunction with a suitable flux limiter. The corresponding solution

efficiency achieved is found to be of O(N), where N is the number of unknowns.

Solutions for spanwise topographies and flow conditions for which corresponding experimental data exists show the two to be in very good agreement with each other and with predictions of the same from corresponding finite-element solutions of the full N-S problem. A subsequent detailed numerical investigation of flow over spanwise step-up and step-down topography, involving varying the step height/depth and Reynolds number range, is used to quantify the accuracy of solutions viz. the depth-averaged equation set. To this end comparisons are made with the N-S solution, taken as the benchmark, and with ones obtained using lubrication theory. The results are summarised as contour plots in one of two ways: (i) the discrepancy which arises, measured relative to the N-S solution; (ii) the relative magnitude of the error associated with the ratio of discrepancies. These clearly show the benefits of the depth-averaged approach over the use of lubrication theory, for increased step-height/depth and Reynolds number, and that the former provides a reasonably good approximation to the flow when compared to its finite element generated counterparts. Furthermore, investigation of the underlying flow structure in the form of streamline plots reveals why a step-down topography leads to a greater maximum error as the step height/depth and Reynolds number become significant, compared to a step-up topography.

For thin film flow over a localised square trench topography, it is found that the general shape of the predicted free-surface disturbance agrees well with its experimentally obtained counterpart, while revealing the subtle effects of increasing inertia. Attention is focused on changes in the characteristic 'horseshoe'-shaped 'bow-wave' and 'comet-tail' features and the effect on the accompanying downstream surge which is not present for flow over spanwise topography. Increased inertia leads to a rise in and sharper focusing of the disturbances in the vicinity of the topography, since streamwise inertia reduces their tendency to spread in the spanwise direction. This finding is consistent with free-surface instabilities arising at critical values of the Reynolds number.

Considered also is the effect of the aspect ratio of the trench topography and substrate inclination angle on the free-surface disturbance as inertia is increased. The results show that despite the tendency of inertia to amplify and focus the associated features, decreasing the inclination angle, and hence the normal component of gravity, suppresses them, with the downstream surge proving to be more resilient to decreasing inclination angle than the upstream bow-wave. Increasing the trench aspect ratio leads to a broadening of the upstream capillary ridge and an eventual bifurcation of the surge; the latter divides to form two decoupled surges and when the aspect ratio is large enough the mid-plane streamwise freesurface profile approaches its spanwise equivalent.

Based on the above observations concerning the effects of inertia apropos the thin film flow over both spanwise and local topography, together with the efficiency of the strategy devised to solve the governing DAF, the methodology is readily extensible for the investigation of a wealth of related three-dimensional flow phenomena. For example, free-surface planarisation with respect to photolithography together with droplet spreading and coalescence on patterned (topographically and/or chemically) surfaces. Furthermore, it is a relatively simple task to include additional physics such as evaporation and thermal effects.

Acknowledgements

S Veremieiev gratefully acknowledges the financial support of the European Union via Marie Curie Action Contract MEST-CT-2005-020599.

Appendix A

Full weighting restriction operators $R^u_{k\to k-1}$ (for u), $R^v_{k\to k-1}$ (for v), $R^h_{k\to k-1}$ (for h):

$$u^{k-1}_{i+1/2,j} = \frac{1}{32}\left[u^k_{2i-1/2,2j-1} + u^k_{2i-1/2,2j+2} + u^k_{2i+3/2,2j-1} + u^k_{2i+3/2,2j+2} + 2\left(u^k_{2i+1/2,2j-1} + u^k_{2i+1/2,2j+2}\right)\right.$$

$$\left. +3\left(u^k_{2i-1/2,2j} + u^k_{2i+3/2,2j} + u^k_{2i-1/2,2j+1} + u^k_{2i+3/2,2j+1}\right) + 6\left(u^k_{2i+1/2,2j} + u^k_{2i+1/2,2j+1}\right)\right],$$

$$v^{k-1}_{i,j+1/2} = \frac{1}{32}\left[v^k_{2i-1,2j-1/2} + v^k_{2i+2,2j-1/2} + v^k_{2i-1,2j+3/2} + v^k_{2i+2,2j+3/2} + 2\left(v^k_{2i-1,2j+1/2} + v^k_{2i+2,2j+1/2}\right)\right.$$

$$\left. +3\left(v^k_{2i,2j-1/2} + v^k_{2i,2j+3/2} + v^k_{2i+1,2j-1/2} + v^k_{2i+1,2j+3/2}\right) + 6\left(v^k_{2i,2j+1/2} + v^k_{2i+1,2j+1/2}\right)\right], \qquad (71)$$

$$h^{k-1}_{i,j} = \frac{1}{64}\left[h^k_{2i-1,2j-1} + h^k_{2i-1,2j+2} + h^k_{2i+2,2j-1} + h^k_{2i+2,2j+2} + 3\left(h^k_{2i,2j-1} + h^k_{2i,2j+2}\right.\right.$$

$$\left. +h^k_{2i+1,2j-1} + h^k_{2i+1,2j+2}h^k_{2i-1,2j} + h^k_{2i-1,2j+1} + h^k_{2i+2,2j} + h^k_{2i+2,2j+1}\right)$$

$$\left. +9\left(h^k_{2i,2j} + h^k_{2i+1,2j} + h^k_{2i,2j+1} + h^k_{2i+1,2j+1}\right)\right].$$

Bilinear interpolation operators $I^u_{k-1\to k}$ (for u), $I^v_{k-1\to k}$ (for v), $I^h_{k-1\to k}$ (for h):

$$u^k_{2i+1/2,2j} = \frac{1}{4}\left[3u^{k-1}_{i+1/2,j} + u^{k-1}_{i+1/2,j-1}\right],$$

$$u^k_{2i+3/2,2j} = \frac{1}{8}\left[3\left(u^{k-1}_{i+1/2,j} + u^{k-1}_{i+3/2,j}\right) + u^{k-1}_{i+1/2,j-1} + u^{k-1}_{i+3/2,j-1}\right],$$

$$u^k_{2i+1/2,2j+1} = \frac{1}{4}\left[3u^{k-1}_{i+1/2,j} + u^{k-1}_{i+1/2,j+1}\right],$$

$$u^k_{2i+3/2,2j+1} = \frac{1}{8}\left[3\left(u^{k-1}_{i+1/2,j} + u^{k-1}_{i+3/2,j}\right) + u^{k-1}_{i+1/2,j+1} + u^{k-1}_{i+3/2,j+1}\right],$$

$$v^k_{2i,2j+1/2} = \frac{1}{4}\left[3v^{k-1}_{i,j+1/2} + v^{k-1}_{i-1,j+1/2}\right],$$

$$v^k_{2i+1,2j+1/2} = \frac{1}{4}\left[3v^{k-1}_{i,j+1/2} + v^{k-1}_{i+1,j+1/2}\right], \qquad (72)$$

$$v^k_{2i,2j+3/2} = \frac{1}{8}\left[3\left(v^{k-1}_{i,j+1/2} + v^{k-1}_{i,j+3/2}\right) + v^{k-1}_{i-1,j+1/2} + v^{k-1}_{i-1,j+3/2}\right],$$

$$v^k_{2i+1,2j+3/2} = \frac{1}{8}\left[3\left(v^{k-1}_{i,j+1/2} + v^{k-1}_{i,j+3/2}\right) + v^{k-1}_{i+1,j+1/2} + v^{k-1}_{i+1,j+3/2}\right],$$

$$h^k_{2i,2j} = \frac{1}{16}\left[9h^{k-1}_{i,j} + 3\left(h^{k-1}_{i-1,j} + h^{k-1}_{i,j-1}\right) + h^{k-1}_{i-1,j-1}\right],$$

$$h^k_{2i+1,2j} = \frac{1}{16}\left[9h^{k-1}_{i,j} + 3\left(h^{k-1}_{i+1,j} + h^{k-1}_{i,j-1}\right) + h^{k-1}_{i+1,j-1}\right],$$

$$h^k_{2i,2j+1} = \frac{1}{16}\left[9h^{k-1}_{i,j} + 3\left(h^{k-1}_{i-1,j} + h^{k-1}_{i,j+1}\right) + h^{k-1}_{i-1,j+1}\right],$$

$$h^k_{2i+1,2j+1} = \frac{1}{16}\left[9h^{k-1}_{i,j} + 3\left(h^{k-1}_{i+1,j} + h^{k-1}_{i,j+1}\right) + h^{k-1}_{i+1,j+1}\right].$$

Appendix B

Coupled equation set solved for the unknown increments $\Delta u_{i+1/2,j}$, $\Delta u_{i-1/2,j}$, $\Delta v_{i,j+1/2}$, $\Delta v_{i,j-1/2}$, $\Delta h_{i,j}$.

$$\begin{aligned}
\frac{\partial \mathcal{N}^u_{i+1/2,j}}{\partial u_{i+1/2,j}}\Delta u_{i+1/2,j} + \frac{\partial \mathcal{N}^u_{i+1/2,j}}{\partial u_{i-1/2,j}}\Delta u_{i-1/2,j} + \frac{\partial \mathcal{N}^u_{i+1/2,j}}{\partial v_{i,j+1/2}}\Delta v_{i,j+1/2} \\
+\frac{\partial \mathcal{N}^u_{i+1/2,j}}{\partial v_{i,j-1/2}}\Delta v_{i,j-1/2} + \frac{\partial \mathcal{N}^u_{i+1/2,j}}{\partial h_{i,j}}\Delta h_{i,j} &= d^u_{i+1/2,j}, \\
\frac{\partial \mathcal{N}^u_{i-1/2,j}}{\partial u_{i+1/2,j}}\Delta u_{i+1/2,j} + \frac{\partial \mathcal{N}^u_{i-1/2,j}}{\partial u_{i-1/2,j}}\Delta u_{i-1/2,j} + \frac{\partial \mathcal{N}^u_{i-1/2,j}}{\partial v_{i,j+1/2}}\Delta v_{i,j+1/2} \\
+\frac{\partial \mathcal{N}^u_{i-1/2,j}}{\partial v_{i,j-1/2}}\Delta v_{i,j-1/2} + \frac{\partial \mathcal{N}^u_{i-1/2,j}}{\partial h_{i,j}}\Delta h_{i,j} &= d^u_{i-1/2,j}, \\
\frac{\partial \mathcal{N}^v_{i,j+1/2}}{\partial u_{i+1/2,j}}\Delta u_{i+1/2,j} + \frac{\partial \mathcal{N}^v_{i,j+1/2}}{\partial u_{i-1/2,j}}\Delta u_{i-1/2,j} + \frac{\partial \mathcal{N}^v_{i,j+1/2}}{\partial v_{i,j+1/2}}\Delta v_{i,j+1/2} \\
+\frac{\partial \mathcal{N}^v_{i,j+1/2}}{\partial v_{i,j-1/2}}\Delta v_{i,j-1/2} + \frac{\partial \mathcal{N}^v_{i,j+1/2}}{\partial h_{i,j}}\Delta h_{i,j} &= d^v_{i,j+1/2}, \\
\frac{\partial \mathcal{N}^v_{i,j-1/2}}{\partial u_{i+1/2,j}}\Delta u_{i+1/2,j} + \frac{\partial \mathcal{N}^v_{i,j-1/2}}{\partial u_{i-1/2,j}}\Delta u_{i-1/2,j} + \frac{\partial \mathcal{N}^v_{i,j-1/2}}{\partial v_{i,j+1/2}}\Delta v_{i,j+1/2} \\
+\frac{\partial \mathcal{N}^v_{i,j-1/2}}{\partial v_{i,j-1/2}}\Delta v_{i,j-1/2} + \frac{\partial \mathcal{N}^v_{i,j-1/2}}{\partial h_{i,j}}\Delta h_{i,j} &= d^v_{i,j-1/2},
\end{aligned} \tag{73}$$

$$\begin{aligned}
\frac{\partial \mathcal{N}^h_{i,j}}{\partial u_{i+1/2,j}}\Delta u_{i+1/2,j} + \frac{\partial \mathcal{N}^h_{i,j}}{\partial u_{i-1/2,j}}\Delta u_{i-1/2,j} + \frac{\partial \mathcal{N}^h_{i,j}}{\partial v_{i,j+1/2}}\Delta v_{i,j+1/2} \\
+\frac{\partial \mathcal{N}^h_{i,j}}{\partial v_{i,j-1/2}}\Delta v_{i,j-1/2} + \frac{\partial \mathcal{N}^h_{i,j}}{\partial h_{i,j}}\Delta h_{i,j} &= d^h_{i,j}.
\end{aligned} \tag{74}$$

Tables

Table 1: Range of flow parameters investigated showing how, for fixed fluid properties, they and the non-dimensional groupings change in concert.

$\theta,^\circ$	Re	$H_0, \mu m$	L_0, mm	$U_0, mm/s$	Ca, 10^{-3}	N	$\mathcal{I}$
30	0.15	39.4	0.572	3.8	0.05	0.07	0.01
30	2.45	100.0	0.781	24.5	0.35	0.12	0.17
30	2.84	105.0	0.794	27.0	0.39	0.13	0.21
30	5	126.8	0.845	39.4	0.56	0.14	0.41
30	15	182.9	0.955	82.0	1.17	0.18	1.58
30	30	230.5	1.032	130.2	1.86	0.21	3.69
30	50	273.3	1.092	183.0	2.61	0.24	6.88
10	5	180.5	1.353	27.7	0.40	0.42	0.37
10	50	388.8	1.747	128.6	1.84	0.69	6.13
5	5	227.0	1.838	22.0	0.31	0.78	0.34
5	50	489.2	2.373	102.2	1.46	1.30	5.67
1	5	388.0	3.754	12.9	0.18	3.25	0.28
1	50	836.0	4.848	59.8	0.85	5.44	4.74

Figures

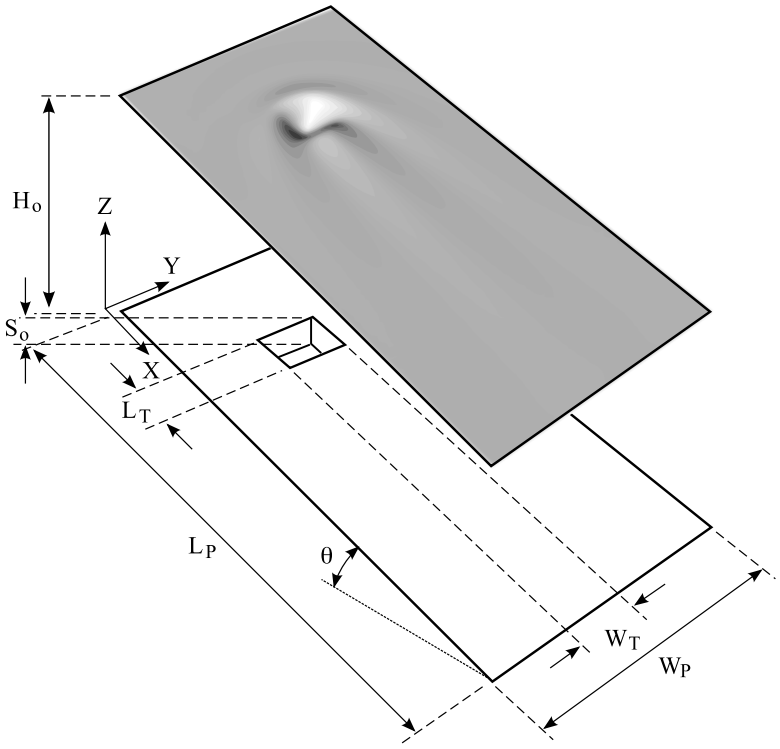

Figure 1: Schematic diagram of gravity-driven flow over a well-defined trench topography, showing the coordinate system adopted and surface geometry.

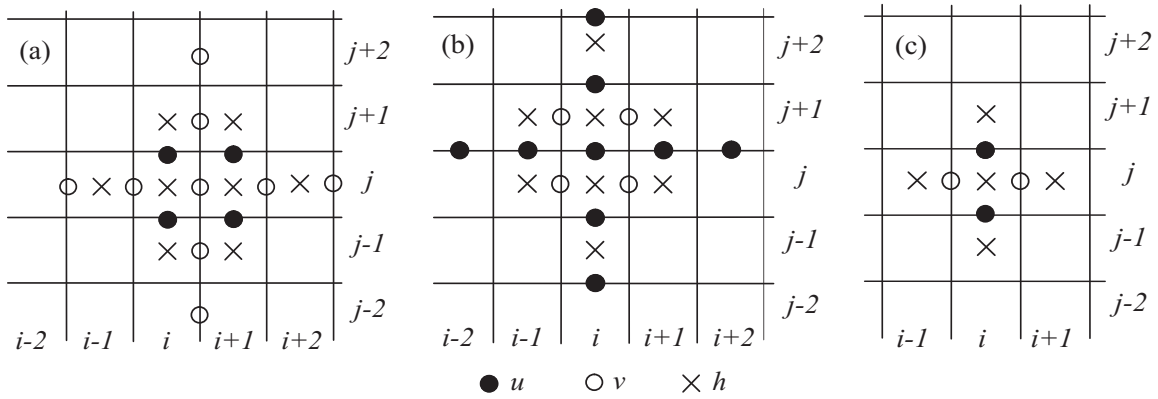

Figure 2: Stencils for defining the functions: (a) $\mathcal{M}^u_{i+1/2,j}$; (b) $\mathcal{M}^v_{i,j+1/2}$; (c) $\mathcal{M}^h_{i,j}$. The positions of the independent variables u, v and h are denoted by open circles, filled circles and crosses, respectively.

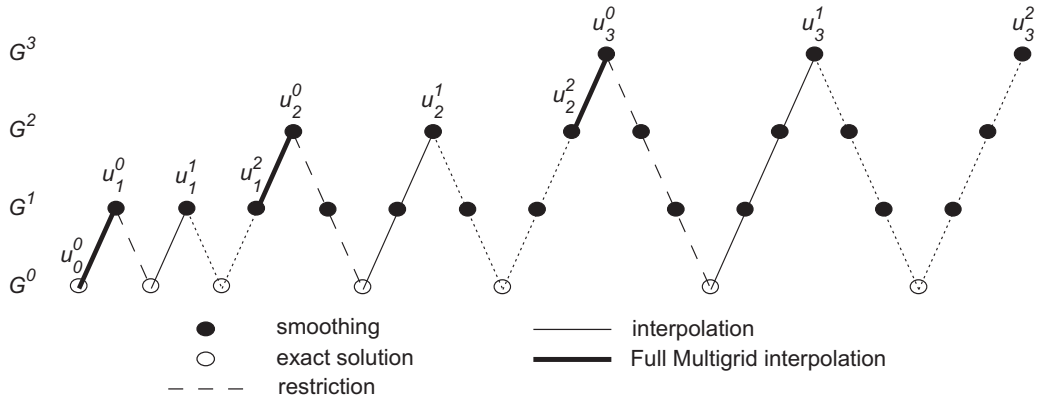

Figure 3: The Full Multigrid structure based, for illustration purposes, on four grid levels. u_0^0 is the initial solution on the coarsest grid provided by the predictor stage, u_k^0 is the solution on the $G^k \in [G^1, G^3]$ grid provided by FMG interpolation; while u_k^1 and u_k^2 is the solution on the $G^k \in [G^1, G^3]$ grid after the first and second FAS V-cycle, respectively.

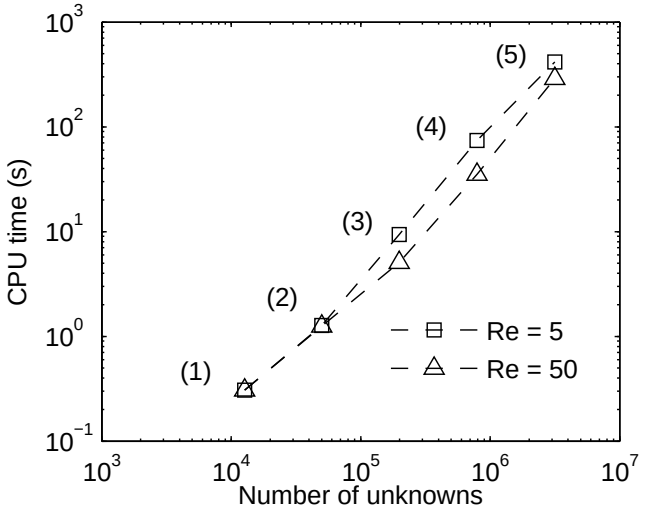

Figure 4: CPU time dependence, for a typical time step, on mesh density, taking threedimensional flow over a localised square trench topography as a benchmark, as per Figs. 12(a) and (d), for the indicated Re values. Mesh density: (1) 64×64; (2) 128×128; (3) 256×256; (4) 512×512; and (5) 1024×1024.

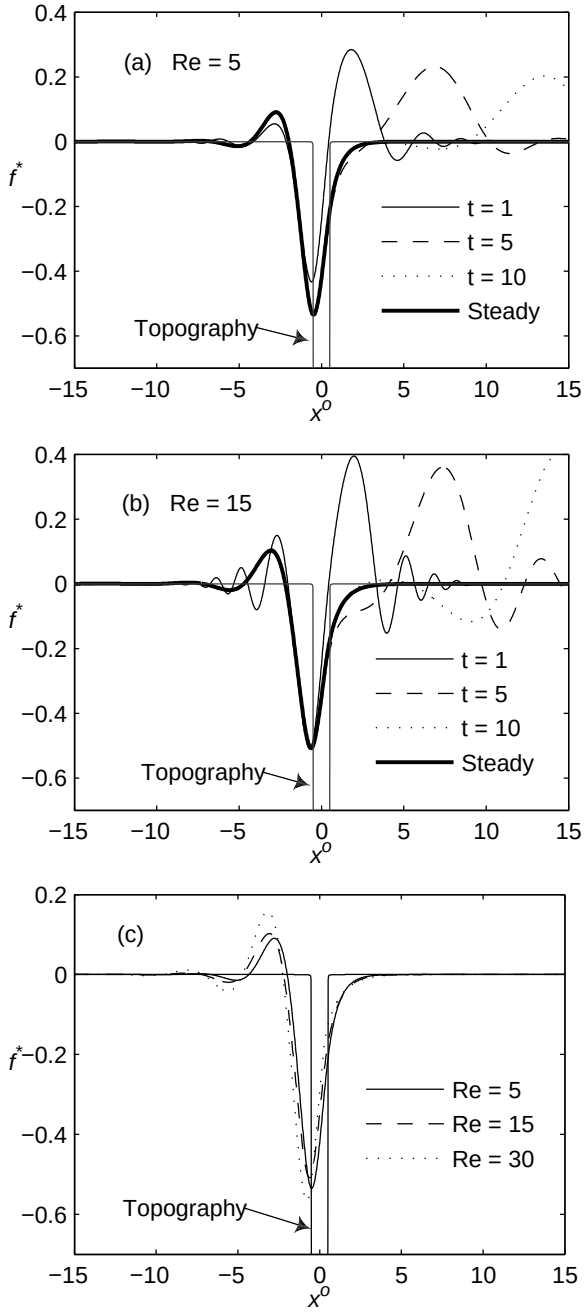

Figure 5: DAF predictions of free-surface profiles for thin film flow over a spanwise trench (width $L_t = 1.2$ mm, depth $S_0 = 20\mu m$): progression from an initial flat surface to predicted steady-state for (a) Re = 5, (b) Re = 15; (c) steady-state solutions for Re $= 5, 15, 30$. The associated trench topography profile, s^*, is as indicated.

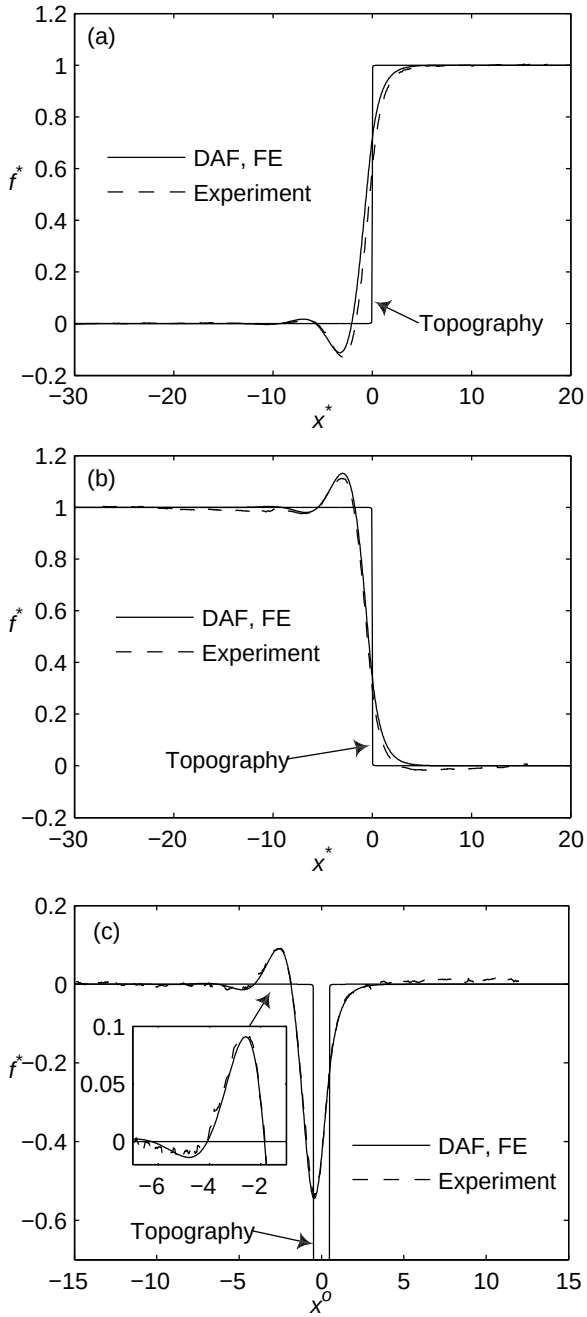

Figure 6: Comparison between predicted (DAF and FE) and experimentally obtained [31] free-surface profiles for thin film flow over a spanwise: (a) step-up (height $|s_0| = 0.2$ and $\mathrm{Re} = 2.45$); (b) step-down (depth $|s_0| = 0.2$ and $\mathrm{Re} = 2.45$); (c) trench topography (depth $s_0 = 0.19$, width $l_t = 1.51$ and $\mathrm{Re} = 2.84$). The associated trench topography profile, s^*, is as indicated.

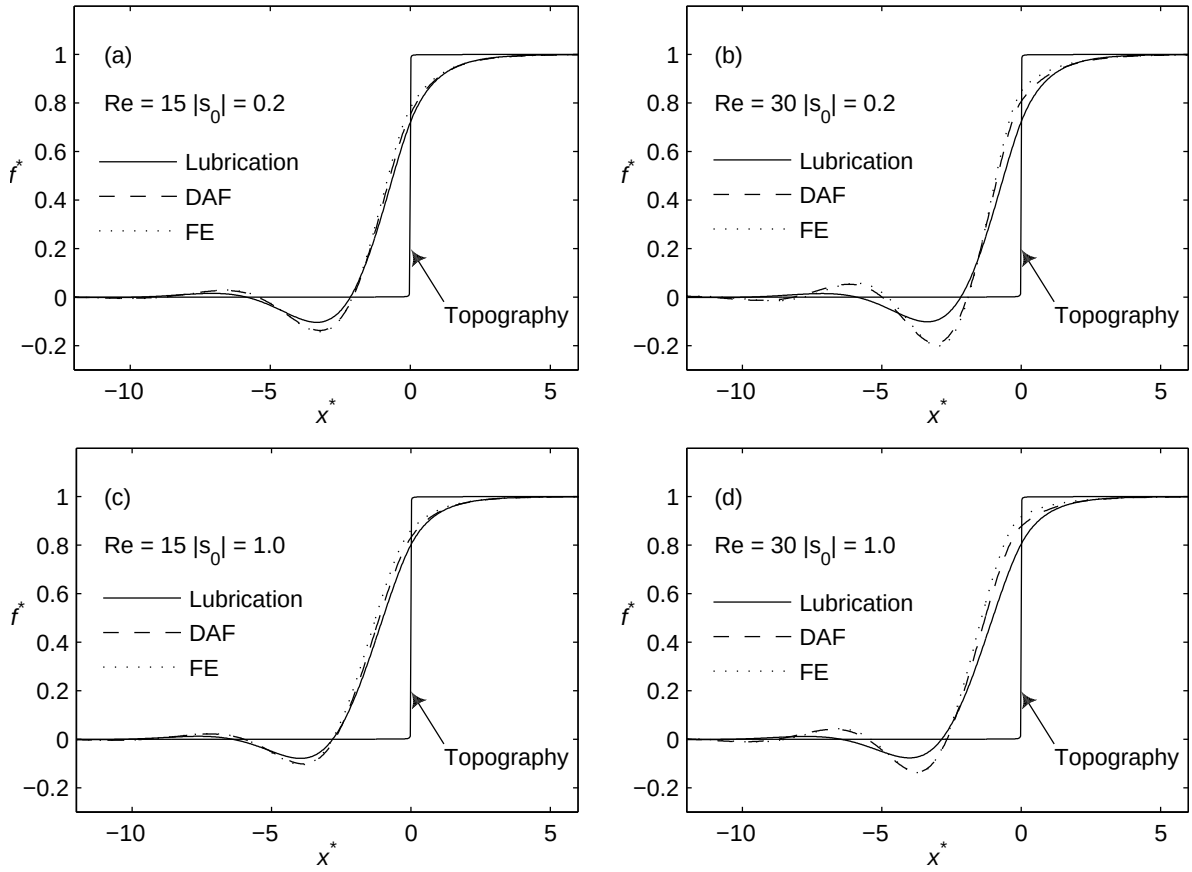

Figure 7: Comparison between predicted (DAF and FE) free-surface profiles for thin film flow over a step-up topography when Re = 15 (left) and 30 (right) for two step heights, $|s_0| = 0.2$ (top) and 1.0 (bottom). The corresponding prediction given by lubrication theory [14] is shown in each case. The topography profile, s^*, is as indicated.

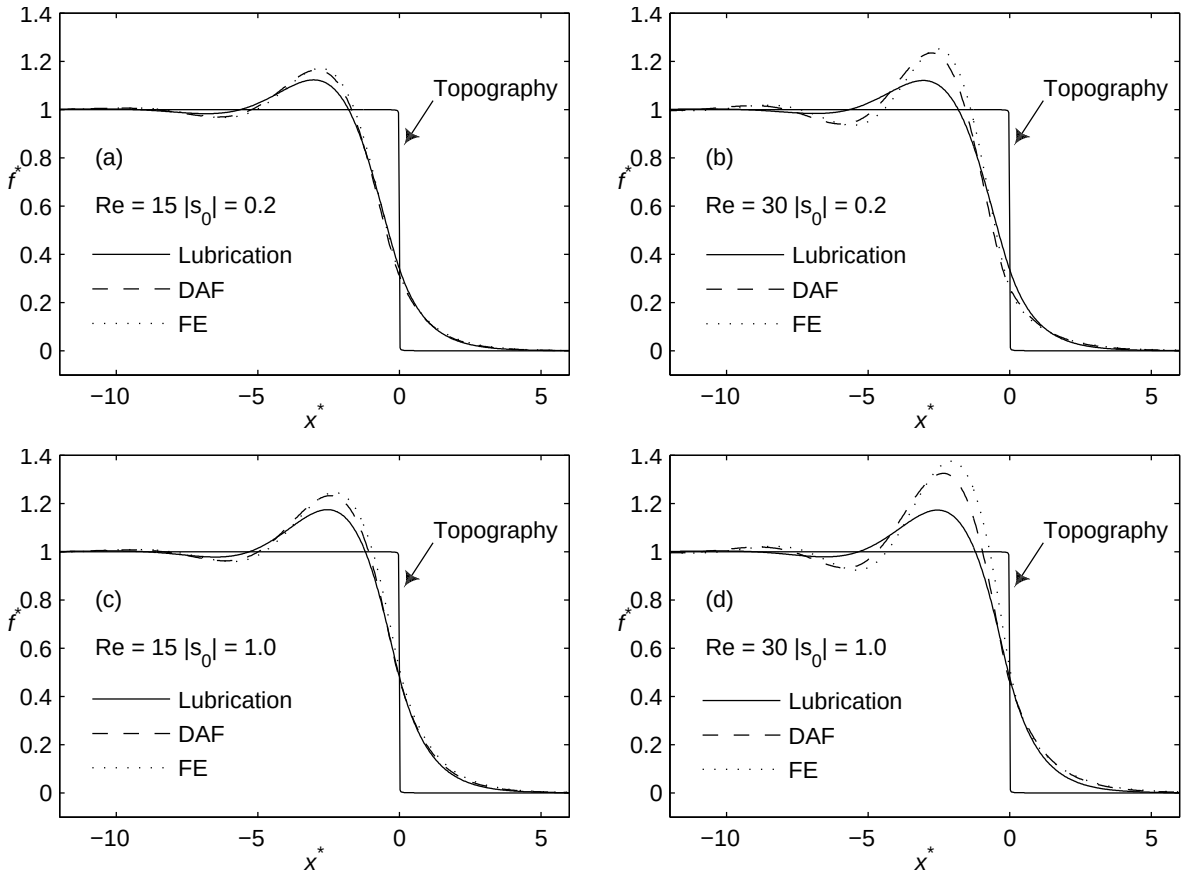

Figure 8: Comparison between predicted (DAF and FE) free-surface profiles for thin film flow over a step-down topography when Re = 15 (left) and 30 (right) for two step heights, $|s_0| = 0.2$ (top) and 1.0 (bottom). The corresponding prediction given by lubrication theory [14] is shown in each case. The topography profile, s^*, is as indicated.

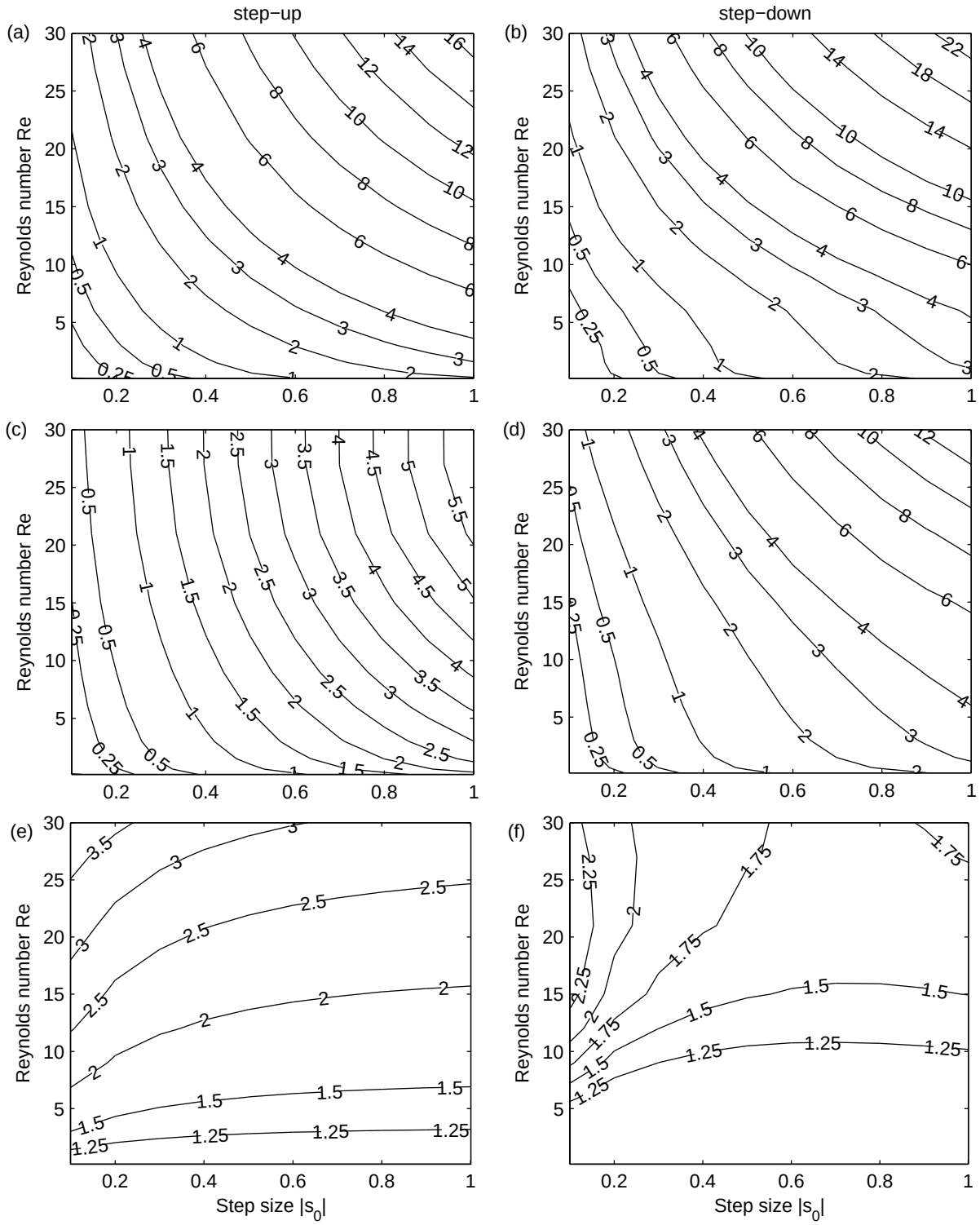

Figure 9: Flow over spanwise step-up (left) and step-down (right) topography with Re $\in [0.15, 30]$ and $|s_0| \in [0.1, 1]$. Contours illustrating the maximum percentage discrepancy in the free-surface profiles obtained with lubrication theory (top) and the DAF (middle), taking corresponding finite element solutions of the full N-S problem as the benchmark. Relative difference in the magnitude of the error expressed as the ratio of solutions obtained via lubrication theory to those found using the DAF (bottom) - for example, a value of 2 indicates the error from lubrication theory to be twice that expected with the DAF.

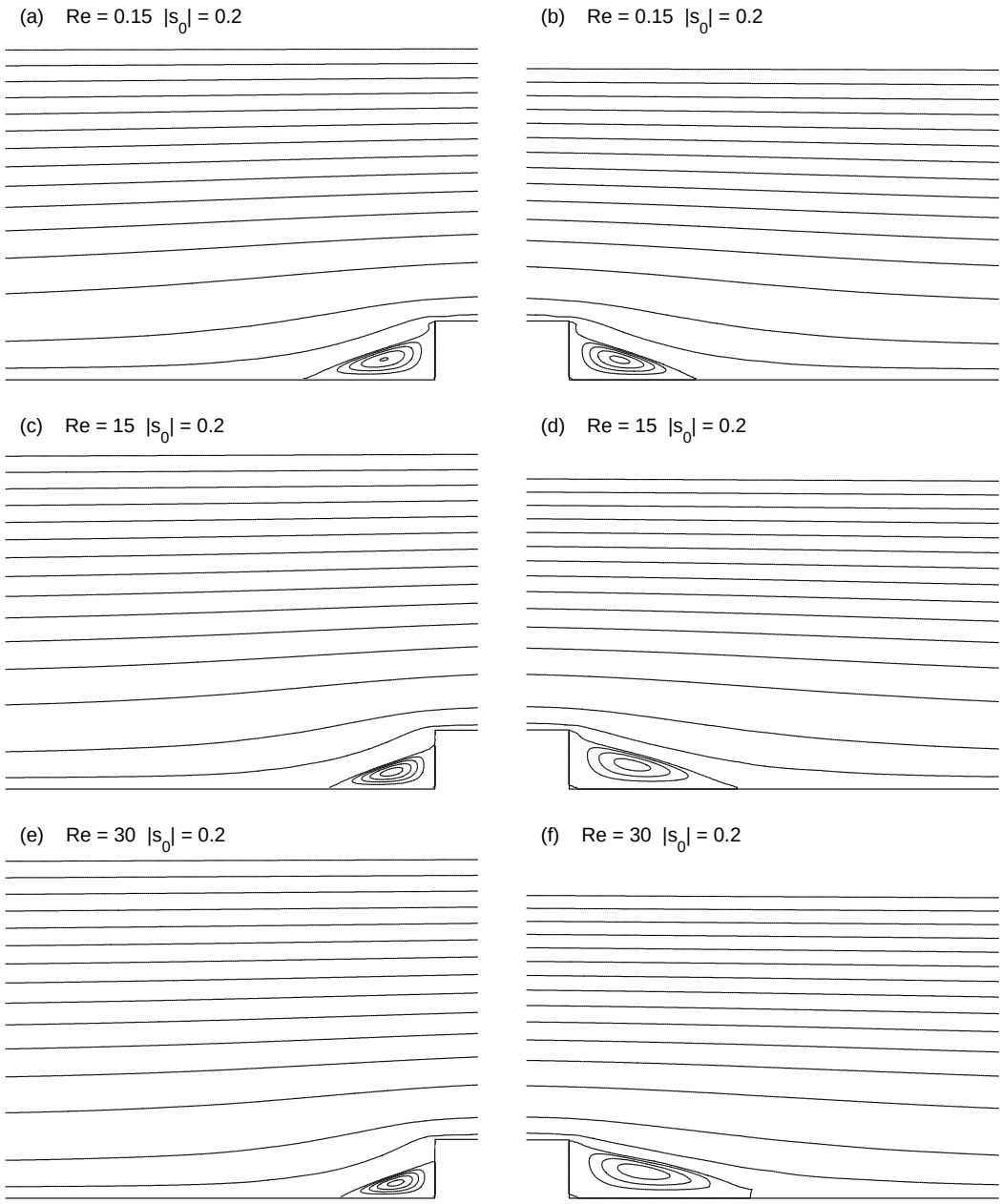

Figure 10: Streamlines showing the effect of inertia on two-dimensional flow over a step-up (left) and a step-down (right) topography, $|s_0| = 0.2$, for: (a),(b) Re = 0.15; (c),(d) Re = 15; (e),(f) Re = 30.

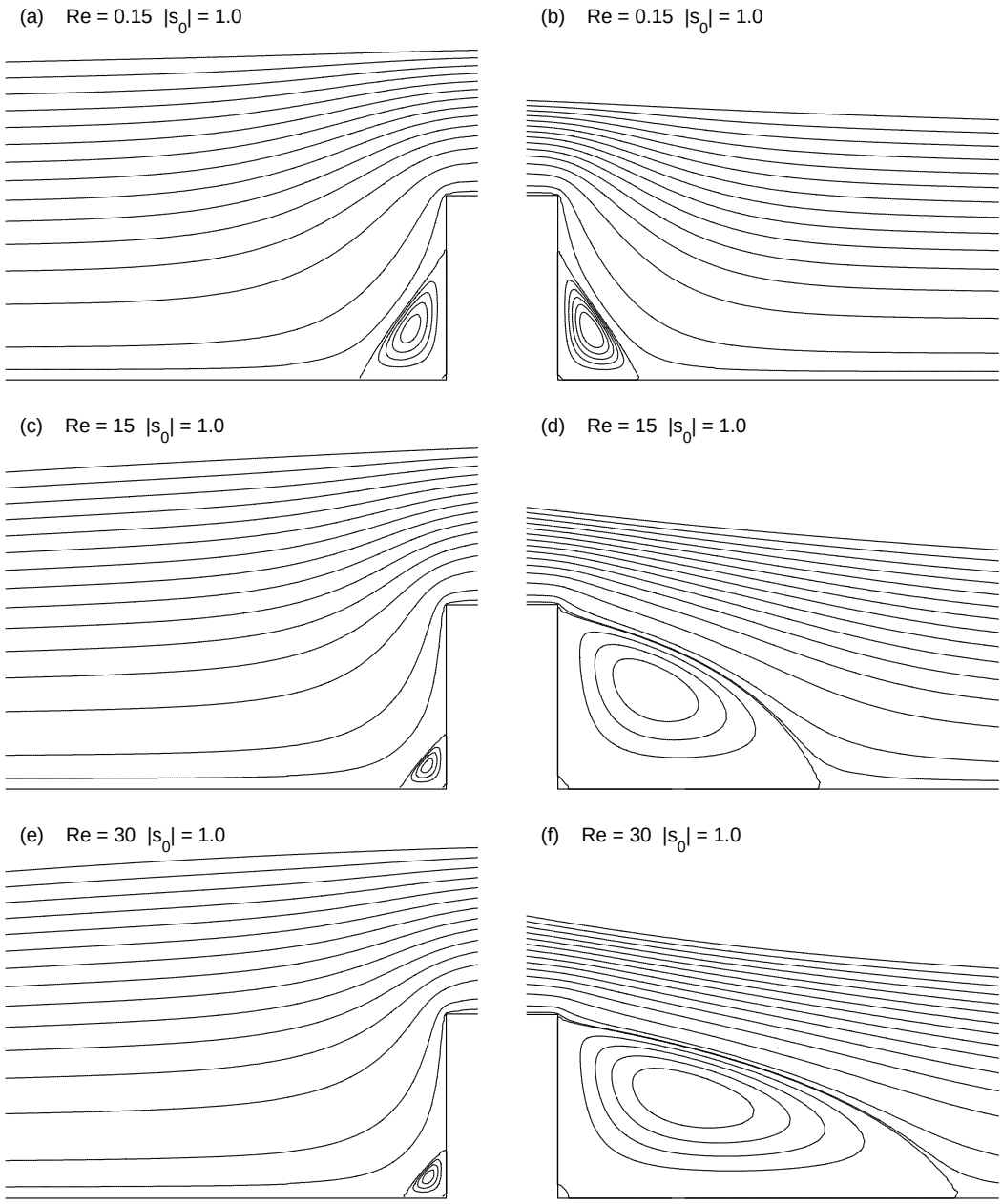

Figure 11: Streamlines showing the effect of inertia on two-dimensional flow over a step-up (left) and a step-down (right) topography, $|s_0| = 1.0$, for: (a),(b) Re = 0.15; (c),(d) Re = 15; (e),(f) Re = 30.

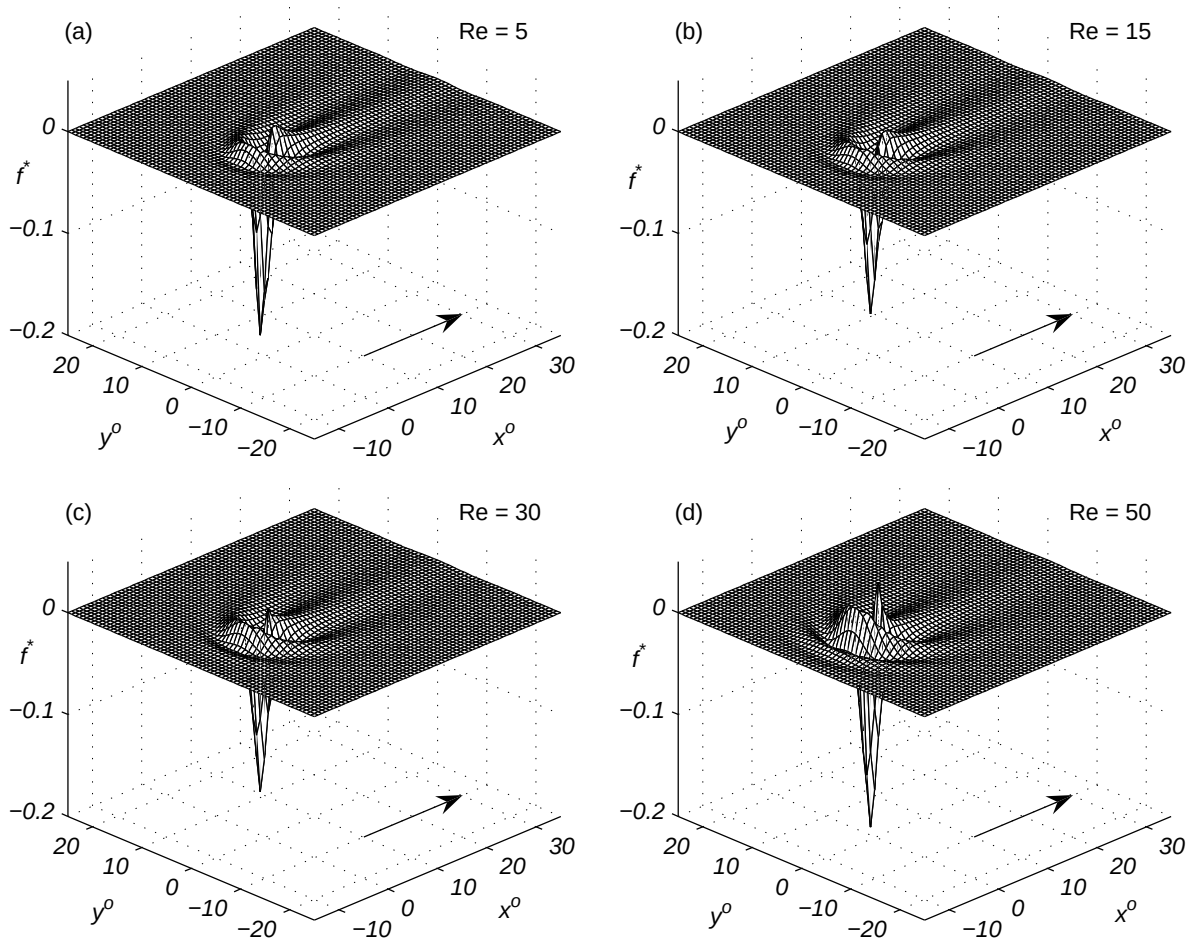

Figure 12: Three-dimensional free-surface plots for flow over a localised (two-dimensional) square trench topography ($L_t = W_t = 1.2mm$, $S_0 = 25\mu m$): (a) Re = 5; (b) Re = 15; (c) Re = 30; (d) Re = 50. The arrow shows the direction of flow.

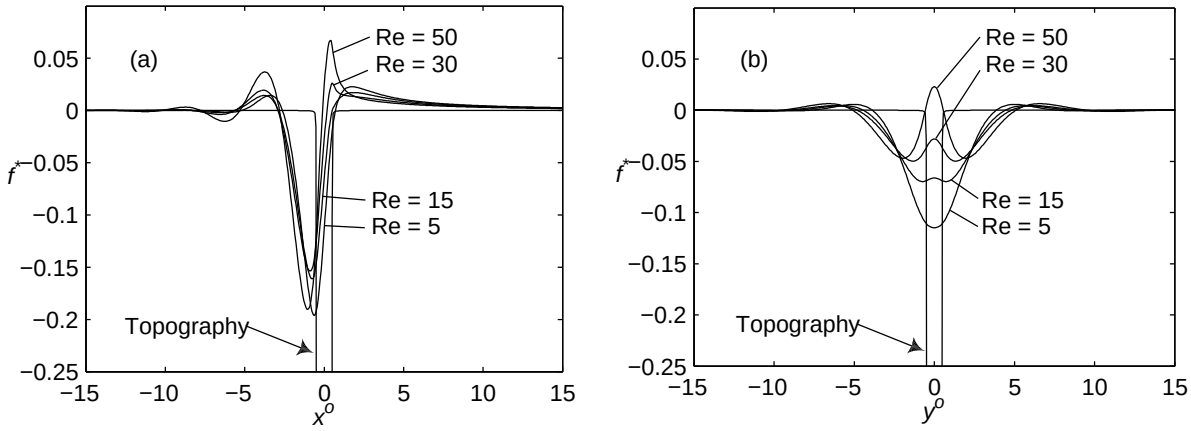

Figure 13: Flow over a localised (two-dimensional) square trench topography ($L_t = W_t = 1.2mm$, $S_0 = 25\mu m$. Streamwise (left) and spanwise (right) free-surface profiles through the centre ($x^o = 0, y^o = 0$) of the topography for Re $= 5, 15, 30$and50. The associated streamwise and spanwise topography profiles, s^*, are as indicated.

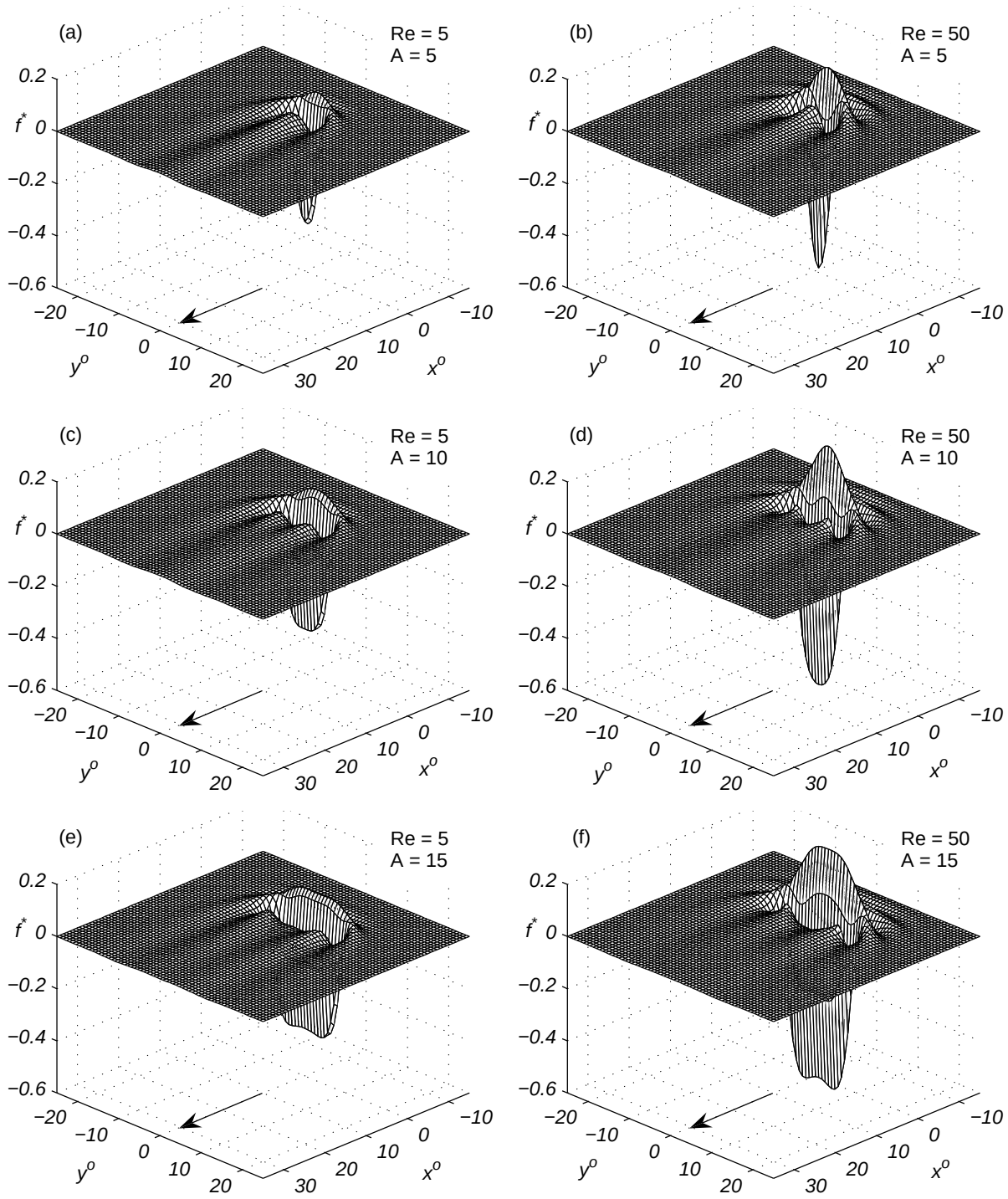

Figure 14: Three-dimensional free-surface plots for flow over a localised trench topography ($L_t = 1.2mm$, $S_0 = 25\mu m$) showing the effect of aspect ratio, $A = W_t/L_t$, on the resulting free surface disturbance. From top to bottom, $A = 5$, 10 and 15; Re = 5 (left) and Re = 50 (right). The arrow shows the direction of flow and the case when $A = 1$ can be viewed in Figs. 11(a) and 11(d).

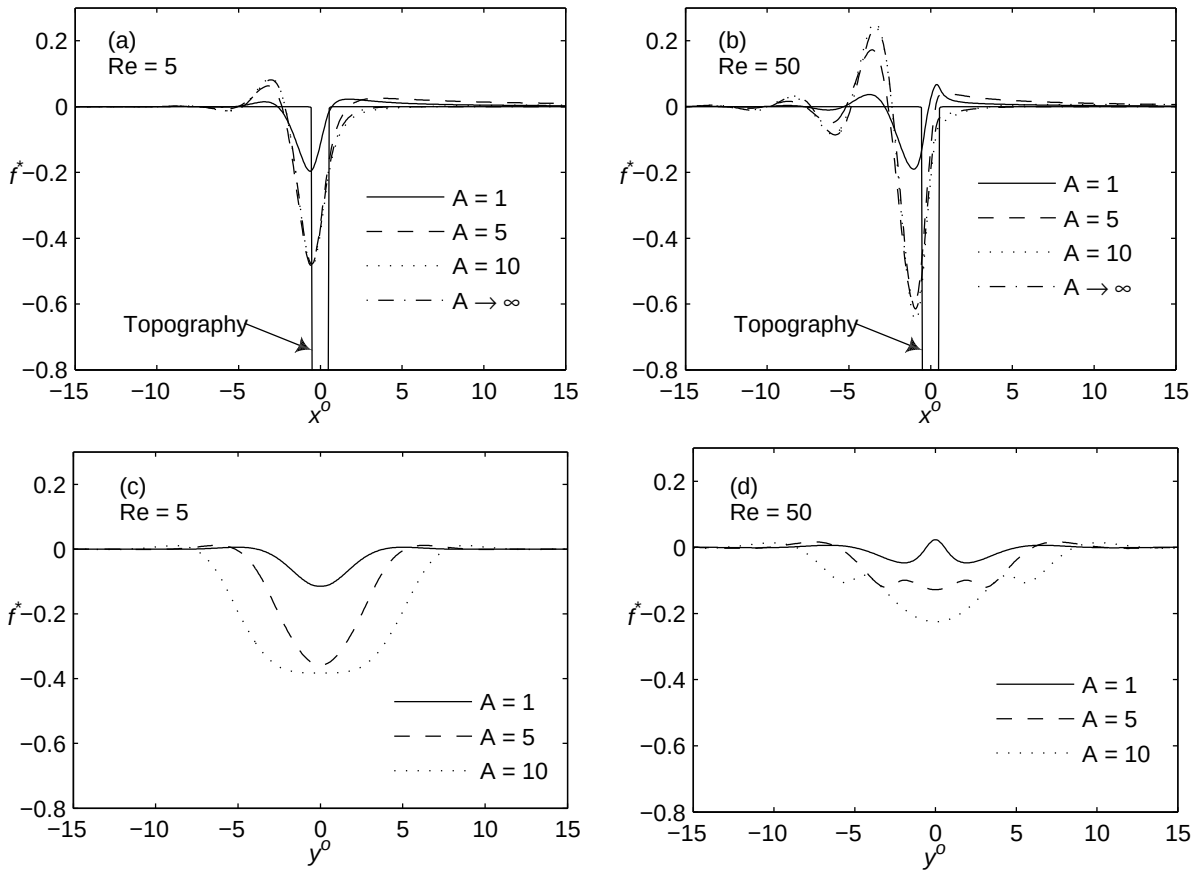

Figure 15: Streamwise (top) and spanwise (bottom) free-surface profiles through the centre of the topography ($x^o = 0, y^o = 0$) for flow over a localised trench topography ($L_t = 1.2mm$, $S_0 = 25\mu m$) showing the effect of aspect ratio, $A = W_t/L_t$ for Re = 5 (left) and Re = 50 (right). The associated streamwise topography profile, s^*, is as indicated.

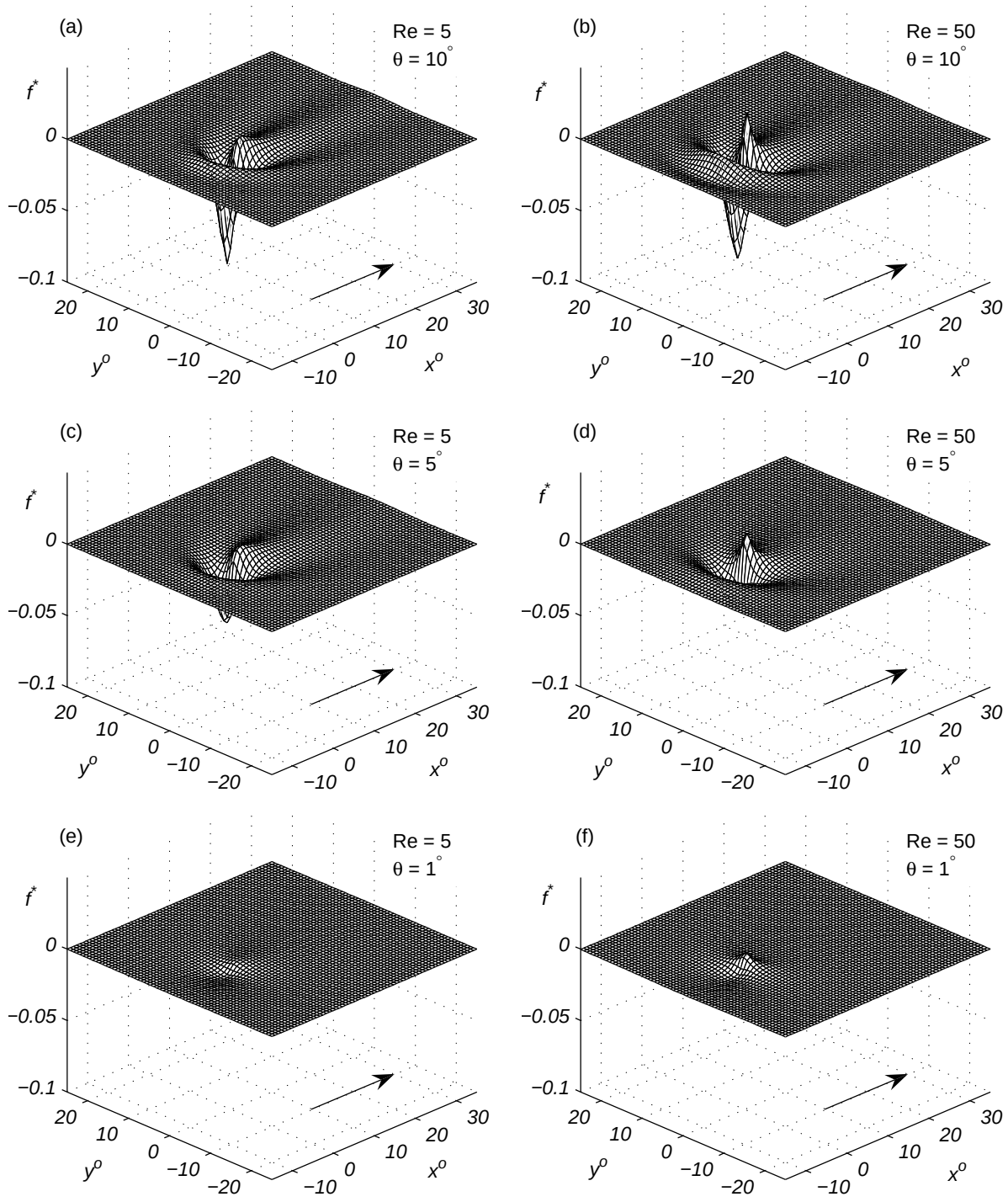

Figure 16: Three-dimensional free surface plots for flow over a localised square trench topography ($L_t = W_t = 1.2mm$, $S_0 = 25\mu m$) showing the effect of θ on the resulting free surface disturbance. From top to bottom, $\theta = 10°,\ 5°$ and $1°$; Re $= 5$ (left) and Re $= 50$ (right). The arrow shows the direction of flow and the corresponding free-surface disturbances when $\theta = 30°$ can be viewed in Figs. 12 (a) and (d).

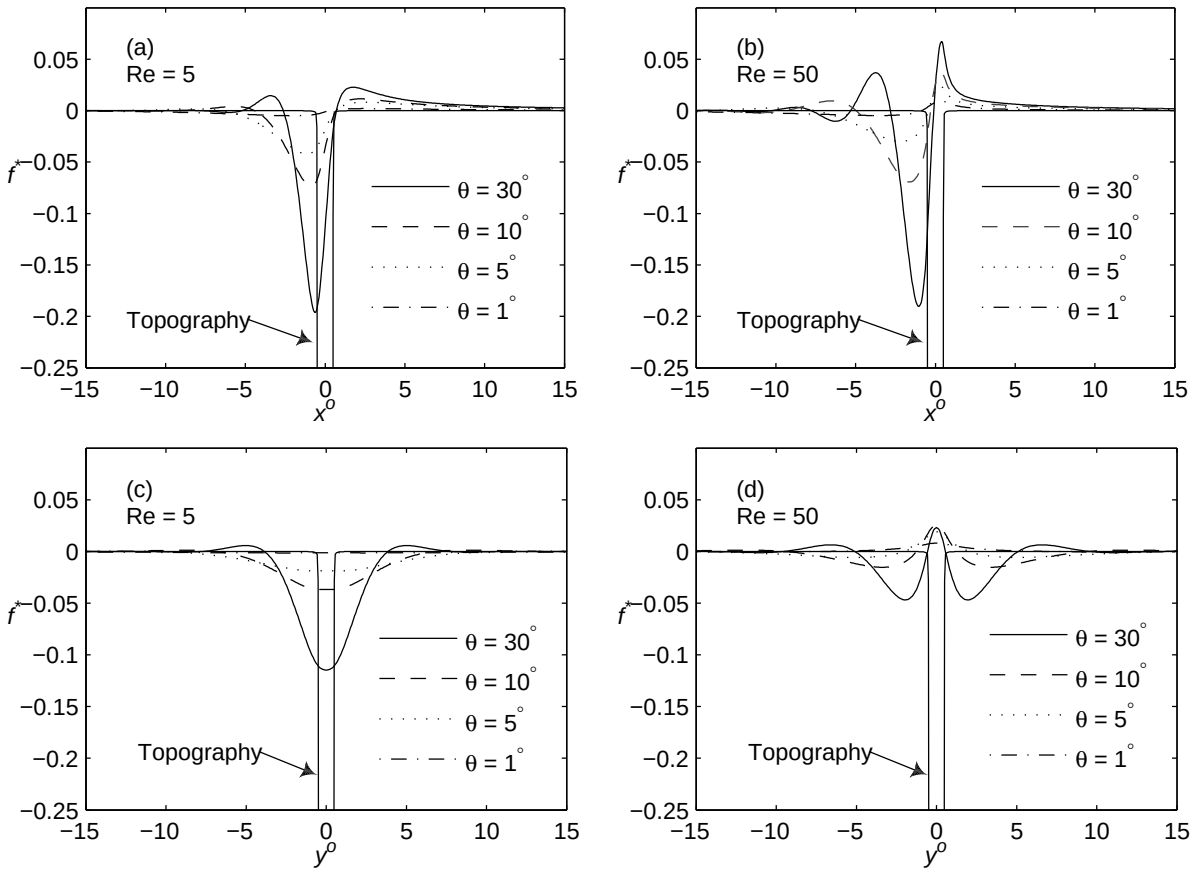

Figure 17: Streamwise (top) and spanwise (bottom) free-surface profiles through the centre of the topography ($x^o = 0, y^o = 0$) for flow over a localised square trench topography ($L_t = W_t = 1.2mm$, $S_0 = 25\mu m$) for four different inclination angles θ; Re = 5 (left) and Re = 50 (right). The associated streamwise and spanwise topography profiles, s^*, are as indicated.

References

[1] S.F. Kistler and P.M. Schweizer, editors. Liquid Film Coating. Chapman and Hall (1997).

[2] P. Tabeling, and S. Cheng, Introduction to Microfluidics. Oxford University Press: Oxford (2005).

[3] J.B. Grotberg, Pulmonary flow and transport phenomena, *Ann. Rev. Fluid Mech.* **26**, 529 (1994).

[4] D.R. Walters, Disguising the leaf surface: the use of leaf coatings for plant disease control, *Euro. J. Plant Path.* **114**, 255 (2006).

[5] H.J. Eberl, and R. Sudarsan, Exposure of biofilms to slow flow fields: the convective contribution to growth and disinfection, *J. Theo. Bio.* **253**, 788 (2008).

[6] S. Lee, J.W.M. Bush, A.E. Hosoi, and E Lauga, Crawling beneath the free surface: water snail locomotion, *Phys. Fluids* **20**, Art. No. 082106, (2008)

[7] S.J. Abbott and P.H. Gaskell, Mass production of bio-inspired structured surfaces, *Proc. I. Mech. E. part C* **221**, 1181 (2007).

[8] A. Oron, S.H. Davis, and S.G. Bankoff, Long scale evolution of thin liquid films, *Rev. Mod. Phys.* **69**, 931 (1997).

[9] C.I. Christov, J. Pontes, D. Walgraef, and M.G. Velarde, Implicit time splitting for forth-order parabolic equations, *Comp. Meth. Appl. Mech. Engrg.* **148**, 209 (1997).

[10] L.W. Schwartz and R.R. Eley, Simulation of droplet motion on low energy and heterogeneous surfaces, *J. Coll. Interface Sci.* **202**, 173 (1998).

[11] N. Daniels, P. Ehret, P.H. Gaskell, H.M. Thompson, and M.M.T. Decré, Multigrid methods for thin film spreading flows, *Proc. 1st Conf. on Computational Fluid Dynamics* (editor N. Satofuka), 279 (2001).

[12] P.H. Gaskell, P.K.Jimack, M. Sellier, and H.M. Thompson, Efficient and accutare time adaptive multigrid solutions of droplet dpreading, *Int. J. Num. Meth fluids* **45,**, 1161 (2004).

[13] P.H. Gaskell, P.K.Jimack, M. Sellier, H.M. Thompson, and M.C.T. Wilson, Gravity-driven flow of continuous thin liquid films on non-porous substrates with topography, *J. Fluid Mech.* 509, 253 (2004).

[14] Y.C. Lee, H.M. Thompson, and P.H. Gaskell, An efficient adaptive multigrid algorithm for predicting thin film flow on surfaces containing localised topographical features, *Comp. Fluids* **36**, 838 (2007).

[15] M. Sellier, Y.C. Lee, H.M. Thompson, and P.H. Gaskell, Thin film flow on surfaces containing arbitrary occlusions. *Comp. & Fluids* **38**, 171, (2009).

[16] P.H. Gaskell, P.K.Jimack, M. Sellier, and H.M. Thompson, Flow of evaporating gravity-driven thin liquid films over topography, *Phys. Fluids* **18**, Art. No. 013601 (2006).

[17] C. Pozrikidis and S.T. Thoroddsen, The deformation of a liquid-film flowing down an inclined plane wall over a small particle arrested on the wall, *Phys. Fluids* **3**, 2546 (1991).

[18] M.G. Blyth and C. Pozrikidis, Film flow down an inclined plane over a three-dimensional obstacle, *Phys. Fluids* **18**, Art. No. 052104 (2006).

[19] H. Luo and C. Pozrikidis, Effect of inertia on film flow over oblique and three-dimensional corrugations, *Phys. Fluids* **18**, Art. No. 078107 (2006).

[20] H. Luo and C. Pozrikidis, Gravity-driven film flow down an inclined wall with three-dimensional corrugations, *Acta Mech.* **188**, 209 (2007).

[21] L.E. Stillwagon, R.G. Larson, and G.N. Taylor, Planarization of substrate topography by spin coating, *J. Electrochem. Soc.* **134**, 2030 (1987).

[22] L.E. Stillwagon and R.G. Larson, Fundamentals of topographic substrate leveling, *J. App. Phys,* **63**, 5251 (1988).

[23] L.E. Stillwagon and R.G. Larson, Leveling of thin films over uneven substrates during spin coating, *Phys. Fluids* **2**, 1937 (1990).

[24] W.G. Pritchard, L.R. Scott, and S.J. Tavener, Numerical and asymptotic methods for certain viscous free-surface flows, *Phil. Trans. Roy. Soc. Series A* **340(1656)**, 1 (1992).

[25] C. Fernandez-Parent, J.H. Lammers, and M.M.J. Decré, Flow of a gravity driven thin liquid film over one-dimensional topographies, *Philips Research, Unclassified Report:* NL-UR 823/98, (1998).

[26] L.M. Peurrung and D.B. Graves, Film thickness profiles over topography in spin coating, *J. Electrochem. Soc.* **138**, 2115 (1991).

[27] L.M. Peurrung and D.B. Graves, Spin coating over topography, IEEE Trans. Semicond. Manu. **6**, 72 (1993).

[28] S. Messé and M.M.T. Decré, Experimental study of a gravity driven water film flowing down inclined plates with different patterns, *Philips Research, Unclassified Report:* NL-UR 030/97 (1997).

[29] M. Lucea, M.M.T. Decré, and J. Lammers, Flow of a gravity driven thin liquid film over one-dimensional Topographies: A detailed comparison of theory and experiments, *Philips Research, Unclassified Report:* NL-UR 823/99 (1999).

[30] J.C. Baret and M.M.T. Decré, Gravity driven flows over two-dimensional topographies: measurement of the free surface using phase stepped interferometry, *Philips Research, Unclassified Report:* NL-UR 829/00 (2000).

[31] M.M.J. Decré and J.C. Baret, Gravity-driven flows of viscous liquids over two-dimensional topographies., *J. Fluid Mech.* **487**, 147 (2003).

[32] Shkadov, V.Y., Wave flow regimes of a thin layer of viscous fluid subject to gravity. IRS Fluid Dynamics, 1967. 2(1): p. 29-34.

[33] Shkadov, V.Y., Wave-flow theory for a thin viscous liquid layer. IRS Fluid Dynamics, 1968. 3(2): p. 12-15.

[34] Saprykin, S., R.J. Koopmans, and S. Kalliadasis, Free-surface thin-film flows over topography: influence of inertia and viscoelasticity. Journal of Fluid Mechanics, 2007. 578: p. 271-293.

[35] Ruyer-Quil, C. and P. Manneville, Modeling film flows down inclined planes. European Physical Journal B, 1998. 6(2): p. 277-292.

[36] Ruyer-Quil, C. and P. Manneville, Improved modeling of flows down inclined planes. European Physical Journal B, 2000. 15(2): p. 357-369.

[37] Ruyer-Quil, C. and P. Manneville, Further accuracy and convergence results on the modeling of flows down inclined planes by weighted-residual approximations. Physics of Fluids, 2002. 14(1): p. 170-183.

[38] Amaouche, M., N. Mehidi, and N. Amatousse, An accurate modeling of thin film flows down an incline for inertia dominated regimes. European Journal of Mechanics B-Fluids, 2005. 24(1): p. 49-70.

[39] Usha, R. and B. Uma, Modeling of stationary waves on a thin viscous film down an inclined plane at high Reynolds numbers and moderate Weber numbers using energy integral method. Physics of Fluids, 2004. 16(7): p. 2679-2696.

[40] Bontozoglou, V. and K. Serifi, Falling film flow along steep two-dimensional topography: The effect of inertia. International Journal of Multiphase Flow, 2008. 34(8): p. 734-747.

[41] Benjamin T.B. Wave formation in laminar flow down an inclined plane. J Fluid Mech 1957;2:554-74.

[42] Yih C.S. Stability of a liquid flow down an inclined plane. Phys Fluids 1963;6:321-34.

[43] Chang C.H. Wave evolution on a falling film. Ann Rev Fluid Mech 1994;26:103-36.

[44] Vlachogiannis, M. and V. Bontozoglou, Experiments on laminar film flow along a periodic wall. Journal of Fluid Mechanics, 2002. 457: p. 133-156.

[45] Wierschem, A., C. Lepski, and N. Aksel, Effect of long undulated bottoms on thin gravity-driven films. Acta Mechanica, 2005. 179(1-2): p. 41-66.

[46] Wierschem, A. and N. Aksel, Instability of a liquid film flowing down an inclined wavy plane. Physica D-Nonlinear Phenomena, 2003. 186(3-4): p. 221-237.

[47] Trifonov, Y.Y., Stability of a viscous liquid film flowing down a periodic surface. International Journal of Multiphase Flow, 2007. 33: p. 1186-1204.

[48] Wierschem, A., et al., Linear resonance in viscous films on inclined wavy planes. International Journal of Multiphase Flow, 2008. 34(6): p. 580-589.

[49] Heining, C., et al., Nonlinear resonance in viscous films on inclined wavy planes. International Journal of Multiphase Flow, 2009. 35(1): p. 78-90.

[50] Khayat, R.E., K.T. Kim, and S. Delosquer, Influence of inertia, topography and gravity on transient axisymmetric thin-film flow. International Journal for Numerical Methods in Fluids, 2004. 45(4): p. 391-419.

[51] Spurk, J.H. and Aksel, N. Fluid Mechanics., Academic Press, Springer (2008).

[52] Landau, L.D. and E.M. Lifshitz, Fluid Mechanics. 1987, Oxford: Pergamon.

[53] M. Hayes, S.B.G. O'Brien, and J.H. Lammers, Green's function for steady flow over a small two-dimensional topography. *Phys. Fluids*, **12(11)**, 2845, (2000).

[54] Y.C. Lee, H.M. Thompson, and P.H. Gaskell, The efficient and accurate solution of continuous thin film flow over surface patterning and past occlusions., *Int. J. Num. Meth. Fluids* **56(8)**, 1375, (2008).

[55] K.W. Morton, Numerical Solution of Convection-Diffusion Problems, Applied Mathematics and Mathematical Computation 12, Chapman and Hall: London (1996).

[56] P.H. Gaskell, and A.K.C. Lau, Curvature-compansated convective-transport - SMART a new boundedness-preserving transport algorithm, *Int. J. Num. Meth. Fluids* **8(6)**, 617, (1988).

[57] U. Trottenberg, C.W. Oosterlee, and A. Schuller, Multigrid. 2001: Academic Press (2001).

[58] T.J. Chung, Computational Fluid Dynamics., Cambridge University Press: Cambridge (2002).

[59] S.C. Chapra, and R.P. Canale, Numerical Methods for Engineers., McGraw-Hill: New York (1998).

[60] J.R. Dormand, Numerical Methods for Differential Equations - a Computational Approach., CRC Press: Boca Raton (1996).

[61] M. Scholle, A. Haas, N. Aksel, M.C.T. Wilson, H.M. Thompson, and P.H. Gaskell, Competing geometric and inertial effects on local flow structure in thick gravity-driven fluid flims, *Phys. Fluids*, **20(12)**, Art. No. 123101 (2008).